Bulk Crystals to Surfaces: Combining X-ray Diffraction and Atomic Force Microscopy to Probe the Structure and Formation of Crystal Interfaces

Michael D. Ward*

Department of Chemical Engineering and Materials Science, University of Minnesota, Amundson Hall, 421 Washington Avenue, Southeast, Minneapolis, Minnesota 55455

Received August 10, 2000

Contents

I. Introduction

Organic crystals play a pivotal role in numerous industries, from commodity chemicals such as dyes and monomer feedstocks to specialty pharmaceuticals and agricultural agents. There also is considerable interest in organic crystals because of solid-state properties typically associated with their inorganic counterparts, such as conductivity, superconductivity, magnetism, and second,harmonic generation. These studies have clearly demonstrated that the *supramolecular* structure of an organic crystal, which is the consequence of very delicate and many times unpredictable intermolecular interactions, influences its solid-state properties dramatically. Attempts to direct this self-assembly into preordained three-dimensional (3-D) architectures is generally referred to as "crystal engineering",[1] a discipline that resides at the nexus of solid-state and supramolecular science.

While there has been substantial attention paid to the three-dimensional structure of organic crystals, the examination of the structure, properties, and reactivity of organic crystal *surfaces* has been rather limited. These surfaces can be described as highly ordered two-dimensional (2-D) arrays of molecules in which specific functional groups are exposed at the crystal surface. In this manner, these surfaces resemble the surfaces created by Langmuir monolayers and Langmuir−Blodgett (LB) mono- and multilayers. However, organic crystal surfaces are generally more rigid, more robust, and more well-defined than the surfaces of Langmuir and LB layers. In the absence of significant reconstruction, the structure of a surface can be surmised from identification of the crystal plane corresponding to an exposed facet and examination of the bulk crystal structure, if it is known. The surface properties of a particular organic crystal face will be governed by the molecular functionalities at the surface. Any crystal will have a minimum of six crystal faces, which may or may not be equivalent depending on symmetry considerations. Consequently,

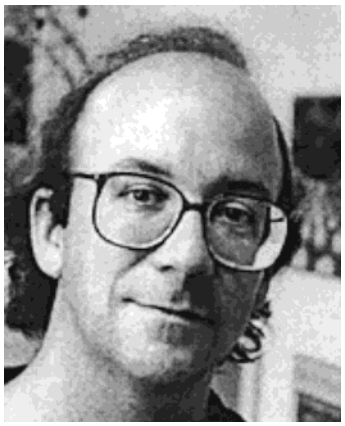

Michael D. Ward received his B.A. degree in Chemistry in 1977 from the William Paterson College of New Jersey and Ph.D. degree in Chemistry in 1981 from Princeton University, and he was a Robert Welch postdoctoral fellow at the University of Texas at Austin from 1981 to 1982. He was a member of the research staff at the Standard Oil Company of Ohio until 1984, when he joined the Dupont Central Research and Development Department in Wilmington, DE. In 1990, he joined the faculty of the Department of Chemical Engineering and Materials Science at the University of Minnesota, where he is now a Distinguished McKnight University Professor. He is also the Director of the University of Minnesota NSF Materials Research Science and Engineering Center and an Associate Editor for *Chemistry of Materials*. His research interests include molecular materials and crystal engineering, physical and electronic properties of molecular solids, nucleation and growth of organic and protein crystals, scanning probe microscopy, and interfacial phenomena.

* To whom correspondence should be addressed. Phone: (612) 625-3062. Fax: (612) 626-7246. E-mail: wardx004@tc.umn.edu.

10.1021/cr000020j CCC: $36.00
Published on Web 04/10/2001

a single crystal exposes numerous surfaces with differing molecular structure. The relative areas of these faces will be governed by their corresponding surface energies, their areas inversely proportional to their relative surface energies (assuming thermodynamic control). The structure and properties of organic crystal surfaces and the molecular organization processes that occur on these surfaces and foreign substrates merit attention for several reasons.

The molecular structures of the faces of a given crystal exert considerable influence over its nucleation and growth, which inherently involve the self-organization of molecules at the exposed surfaces of the crystal. The surface energy of specific crystal planes, which in turn depends on the orientation of the molecules exposed at the surfaces of these planes, affects the distribution of terraces, ledges, and kinks, which represent nanoscopic versions of these planes. The interaction of solvent, additives, and impurities with molecules protruding from these planes can influence crystal morphology, which can be important with respect to crystal properties and the efficiency of industrial scale processes. Elucidating the structure and dynamic behavior of these features is crucial to understanding and improving crystallization processes.

Organic crystal surfaces may serve as substrates for a variety of processes, including controlled epitaxial nucleation and growth of other organic, inorganic, or polymer crystals. Public domain literature and, undoubtedly, internal documents in industrial laboratories abound with examples of crystal seeding for controlled crystallization of small molecule organics and polymers. These seeding processes almost certainly involve epitaxial interfacial interactions between crystal faces and incipient nuclei. If one considers that there are nearly 150 000 entries in the Cambridge Structural Data Base, the variety of available substrate surfaces for nucleation is quite astounding. Crystal seeding strategies based on rational molecular-level concepts using organic crystal surfaces may be possible. These may enable control of selectivity toward particular crystal polymorphs, which can be important in materials processing and applications. For example, polymorphism remains a critical issue in pharmaceuticals, as different crystal forms can exhibit different purity and bioavailabity that affects performance and licensing approval by regulatory agencies.

Organic crystals and related organic films have a promising future in electronic, optoelectronic, and magnetics applications owing to the diverse variety of materials that are possible through organic synthesis. A substantial amount of effort is being spent on the development of organic films for liquid crystal displays and switches, electroluminescent displays, and second-harmonic generation. The properties of such films depend strongly on their structure and the orientation of molecules with respect to the substrate upon which they are fabricated. In the case of crystalline substrates, epitaxy can play an important role in governing the assembly of crystalline organic films.

To a large extent, elucidation of the role of organic crystal surfaces in many of these processes has been frustrated by the absence of suitable experimental methods. However, recent advances in surface characterization techniques such as scanning probe microscopy have provided substantial insight into the structure of organic crystal surfaces. In many cases, these techniques can provide some 3-D structural characterization when single-crystal X-ray diffraction is not possible. The purpose of this paper is to describe, through specific examples, recent advances in scanning probe microscopy that address the structure and properties of selected organic crystal surfaces and the molecular organization processes at those surfaces that govern formation of two- and three-dimensional crystals.

II. Organic Crystal Surfaces

A. Dimensionality, Energetics, and Relationship to Bulk Crystal Structures

Single-crystal X-ray diffraction commonly is used for the determination of molecular structure, particularly when molecular conformations and absolute configurations need to be assigned. However, efforts in crystal engineering over the last three decades have shifted X-ray diffraction studies toward elucidating the supramolecular motifs present in the three-dimensional lattice. These efforts have revealed that predicting solid-state structure is difficult owing to the large number of weak noncovalent intermolecular interactions that govern the assembly of the molecular constituents. Examination of organic crystal structures reveals a diverse variety of supramolecular motifs which can be classified according to their dimensionality, that is, as one-dimensional chains, two-dimensional layers, or three-dimensional networks.[2,3] The dimensionality of most organic crystals can be described according to a hierarchy of intermolecular bonding strength. Many organic crystals exhibit rather well-defined, robust layering motifs in which strong interactions prevail along at least two coordinates within the layer. In these cases, the assembly of these layers along the remaining third dimension by weak van der Waals interactions generates the three-dimensional structure in the bulk crystal. In this respect, organic crystals resemble multilayer Langmuir−Blodgett films but with greater ordering in the third dimension.

The layered nature of these crystals commonly leads to *macroscopic* crystal morphologies in which the largest crystal face is formed from the plane containing the two-dimensional layers, with the area of the remaining faces depending inversely on their surface energy. The predominance of faces containing robust molecular layers can be understood from surface energy considerations, as the crystal plane with the strongest intralayer bonding is likely to have the lowest surface energy. This can be illustrated by α-glycine, which is composed of hydrogen-bonded (HB) bilayers in the {010} plane (Figure 1).[4] Single crystals of α-glycine have large {010} faces, with {011} faces being the next largest. This is consistent with surface energy ranking, as the {010} faces can

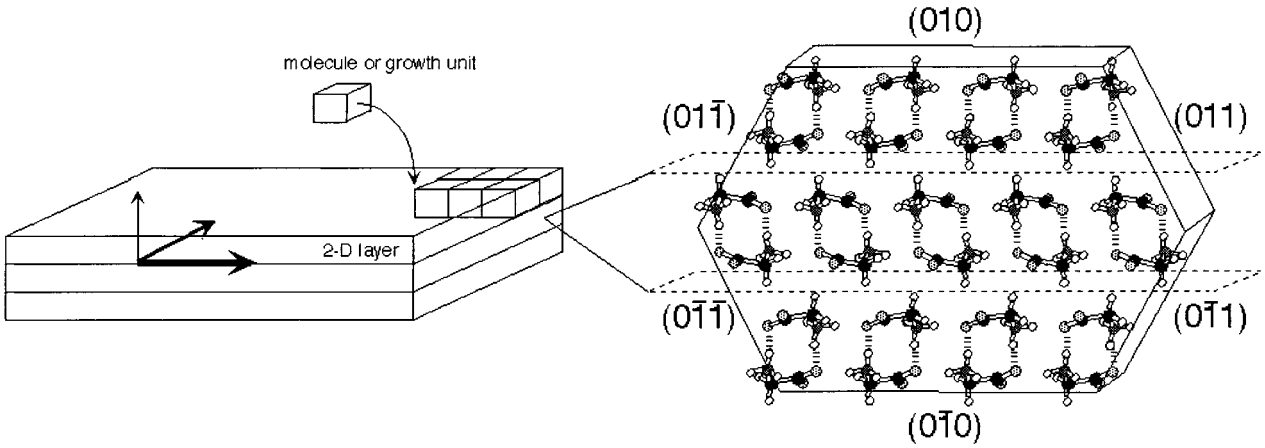

Figure 1. Schematic representation of layering and layer stacking in organic crystals. Each layer consists of molecules or "growth units" held together within the layer by noncovalent intermolecular interactions. The width of the arrows represent the hierarchy of intermolecular bonding, with their widths proportional to the bonding strength. In this example, the 2-D layer has two strong bonding vectors while the bonding between the layers is weak by comparison. Glycine, depicted on the right, consists of hydrogen-bonded bilayers with van der Waals interactions between the bilayers. The hydrogen bonds between glycine molecules across the width of the bilayer are depicted as dashed lines. The hydrogen bonds in the single layers of glycine molecules are not shown. The two planes with dashed boundaries separate the methylene groups projecting from each bilayer.

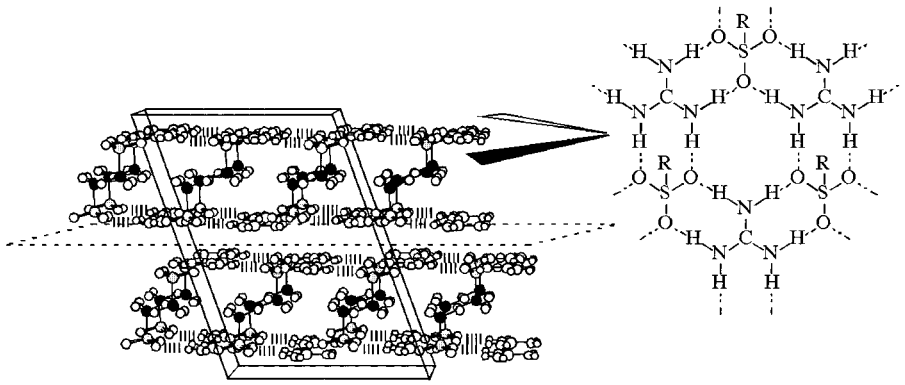

Figure 2. Two (001) bilayers of crystalline guanidinium triflate, each bilayer formed by dispersive interactions between $-CF_3$ groups projecting from opposing hydrogen-bonded sheets. The plane with the dashed outline separates the two bilayers. The carbon atoms of the triflate ion are shaded black and the sulfur atoms gray. The quasihexagonal hydrogen-bonding motif of the 2-D sheets is illustrated.

be terminated with low-energy methylene groups while the {011} faces must be terminated with unsatisfied hydrogen-bonding functionalities (either $-COO^-$ or $-NH_3^+$ groups). This example illustrates that a single crystal can provide numerous surfaces with differing chemical composition and molecular topography. It is also important to note that many layered organic crystals commonly can be cleaved, similar to mica and graphite, to expose the layered planes with well-defined molecular structure.

The hierarchy of intermolecular interactions in organic crystals can generally be deduced by inspection of the single-crystal X-ray structures and the types of interactions along different coordinates. Layering motifs are common for a diverse variety of crystals held together by hydrogen-bonding, charge-transfer, and strong dispersive interactions between chalcogenides such as sulfur and selenium. For example, guanidinium organosulfonates crystallize into layered materials in which the six protons of guanidinium cations and six lone pairs of electrons on the sulfonate moiety assemble into an extremely robust quasihexagonal sheet (Figure 2).[5] These layers then assemble into bilayers by dispersive interaction between the alkyl groups protruding from opposing hydrogen-bonded sheets. The organic conductor β-bis-(ethylenedithiolotetrathiafulvalene)$_2I_3$ (β-(ET)$_2I_3$) organizes as alternating layers of ET molecules, in which each ET molecule carries an average charge of 0.5+ and I_3^- anions. The ET molecules are held together in each layer by strong charge-transfer interactions along stacks combined with strong S$\cdots$S dispersive interactions between the stacks (Figure 3).

In each of these examples the layering motif is easily identified by the segregation of molecules or portions of molecules. Notably, these compounds form platelike crystals with the two-dimensional layers defining the largest crystal face as expected from surface energy rankings. *By definition, the lowest energy surface is the one in which the weakest bonds are truncated as this minimizes the energetic penalty associated with the lack of bonding at this plane.* Consequently, planes that intersect the hydrogen-bonding network in the guanidinium organosul-

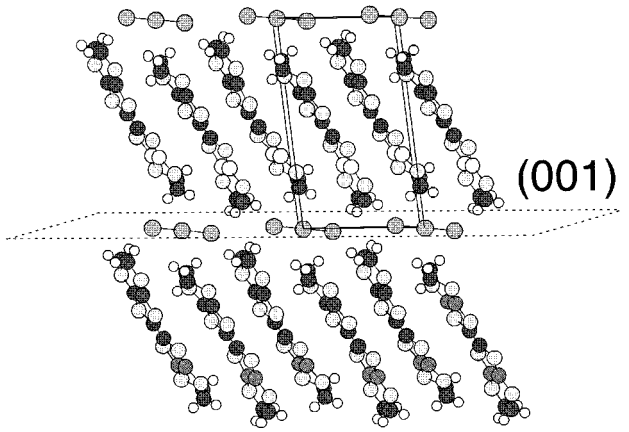

Figure 3. Alternating two-dimensional (001) layers of ET and I_3^- in β-$(ET)_2I_3$. The ET molecules, which each have an average charge of 0.5+, are held together in the layers by charge-transfer interactions (along the horizontally oriented stacks) and dispersive S···S interactions between stacks (along a direction normal to the plane of the paper.

fonates or the 2-D layers of ET molecules in (β-$(ET)_2I_3$ will have high surface energies.

B. Structure Characterization

1. X-ray Diffraction of Crystal Surfaces

The structure of organic crystal surfaces usually can be deduced from the bulk crystal structure, provided the crystal faces can be assigned to their respective Miller planes, usually through X-ray methods or optical goniometry. However, in some cases the surface structure cannot be unequivocally assigned. During the past decade, considerable advances have been made in grazing incidence X-ray diffraction that have provided substantial insight into the structure of crystal surfaces. This technique has also been used extensively for the structural characterization of Langmuir−Blodgett mono- and multilayers and Langmuir monolayers, which over 10 years ago were shown to have structures that resemble their three-dimensional crystalline counterparts. For example, amphiphiles consisting of long alkane chains appended to amino acid groups organize at the air−water interface into structures that mimic the structure of amino acids such as glycine.[6,78]

Like many amino acids, α-glycine and β-alanine consist of centrosymmetric {010} bilayers constructed from dimers of zwitterionic molecules interlinked through strong N−H···O hydrogen bonds (Figure 1). In the case of α-glycine, for example, the {010} faces may be terminated by methylene groups or hydrogen-bonding functionalities. Grazing incidence X-ray diffraction (GIXD) studies, specifically the specular and off-specular crystal truncation rods associated with diffraction from the (010) surfaces, were used to probe the in-plane molecular structure of these crystals.[9,10] The data were consistent with surfaces terminated with the hydrophobic $-CH_2-$ or $-CH(CH_3)-$ groups for α-glycine or β-alanine, respectively. Additionally, the stereospecific adsorption on the (010) face of α-glycine revealed the formation of an ordered (*S*)-methionine/glycine heterobilayer. These observations confirmed the importance of surface energy minimization wherein the weakest intermolecular bonds are truncated at the crystal surface.

GIXD was also used to probe the growth and dissolution interfaces of β-alanine and α-glycine.[11] No change in surface structure was observed during these processes, suggesting that the growth and dissolution occurred bilayer-by-bilayer at the step edges. That is, both alanine and glycine effectively dock or leave the crystal surfaces of β-alanine and α-glycine as cyclic, hydrogen-bonded dimers (which traverse the bilayers) instead of monomers, presumably because the dimers are less solvated and therefore have a greater propensity to attach to the surface. Interestingly, this observation may explain the polymorphism behavior of glycine. Whereas the α form contains glycine dimers in the centrosymmetric (010) bilayers, dimers do not exist in the γ form. Because only one polymorph can represent the thermodynamic minimum at a given temperature and pressure, kinetics plays an important role and, consequently, the speciation of the solute molecules can be critical to polymorph selectivity. In the case of glycine, the γ form crystallizes from either acidic or basic solutions in which dimer structure is disrupted. Under these conditions, crystallization of the α-form would be less favorable than at intermediate pH values where the zwitterionic dimers would be favored. The observation of cyclic dimers crystallizing on (010) α-glycine illustrates that the growth of this polymorph is best achieved under conditions where the dimers are favored.

GIXD also can be employed to elucidate the influence of solvent on crystal growth, which is an important technological issue for numerous industries and of vital fundamental importance to an understanding of the molecular recognition events responsible for crystal nucleation, growth, polymorphism, and morphology. Crystallization of benzamide from ethanol or 1-propanol solutions affords rectangular (001) plates extended in the *b* direction, but in the presence of an amide cosolvent such as CH_3-CONH_2 or CF_3-CONH_2, *very thin* twinned (001) plates were formed.[12] The crystal structure of benzamide reveals (001) bilayers consisting of dimers connected by N−H···O hydrogen bonds. GIXD from the (001) surface of pure benzamide indicates that this surface almost exclusively exposes the phenyl substituents. The formation of very thin (001) plates in the presence of the cosolvent is consistent with inhibition of growth along the *c* direction, which may be explained by stereospecific adsorption of the amide cosolvent through hydrogen bonding to benzamide on the (001) face, with the group −X emerging from the face. Twinning occurs about the *ab* plane, as verified by clearly separated (*h*00) reflections in scans measured on a conventional four-circle diffractometer. Notably, the (10*l*) and (10−*l*) rods obtained by GIXD from the (001) surface of pure benzamide crystal ($1 \leq l \leq 8$) were not equal in intensity, consistent with the $P2_1/c$ space group symmetry. Conversely, crystals grown with acetamide or trifluoroacetamide cosolvents exhibited approximately equal (10*l*) and (10−*l*) intensities, consistent with the presence of lamellar twinned crystallites.

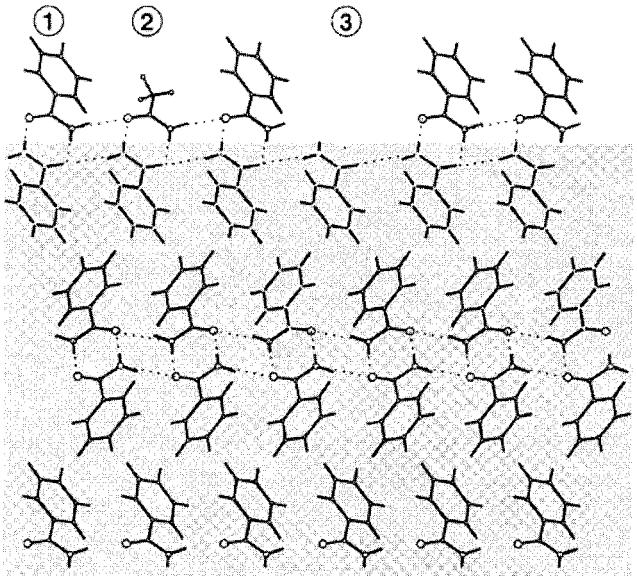

Figure 4. Bulk and surface models used for crystal truncation rod calculations of the pure and affected benzamide crystals. For modeling purposes, the top surface layer was occupied by either (1) the benzamide molecule, (2) the amide cosolvent, or (3) a vacancy. (Reprinted with permission from ref 12. Copyright 1999 American Chemcial Society.)

The crystal truncation rods were measured from the solution-exposed (001) face of a series of benzamide crystal plates, including the pure form grown from 1-propanol and crystals grown with an equimolar concentration of either acetamide or trifluroacetamide. The specular (00*l*) CTRs, which were very sensitive to the nature of the surface layer and depended only on the atomic *z*-coordinates, were fitted to model structures (Figure 4) consisting of the underlying bulk molecular arrangement, taken from the published crystal structure of benzamide and a surface model that accounted for structural variations. The bulk model was terminated with a (001) layer of benzamide exposing amide groups, whereas the surface model consisted of a layer decorated with either pure benzamide, benzamide plus the amide cosolvent (with $-CH_3$ or $-CF_3$ exposed to air), or vacancies. The observed dip in intensity of the (00*l*) truncation rod from the pure benzamide crystal (Figure 5a) at $I \approx 2.2$ signifies a surface layer terminated essentially by phenyl rings, as evinced from calculated intensity profiles for the (001) face exposing a complete layer of phenyl rings or amide groups (Figure 5e). The data were best-fitted with a model in which the surface layer of benzamide has an occupancy of 95% and the remaining 5% of the (001) face terminated with exposed amide groups from the layer below. This result is in agreement with a model in which the crystal growth unit is composed of the cyclic hydrogen-bonded dimer. The sharp Bragg peaks in Figure 5 at l = odd are glide-symmetry forbidden, which suggested a continuous reduction in layer occupancy upon reaching the top surface.

The (00*l*) CTRs from a crystal of benzamide grown from an acetamide−alcohol solvent mixture (Figure 5c) and from the alcohol solvent were found to be

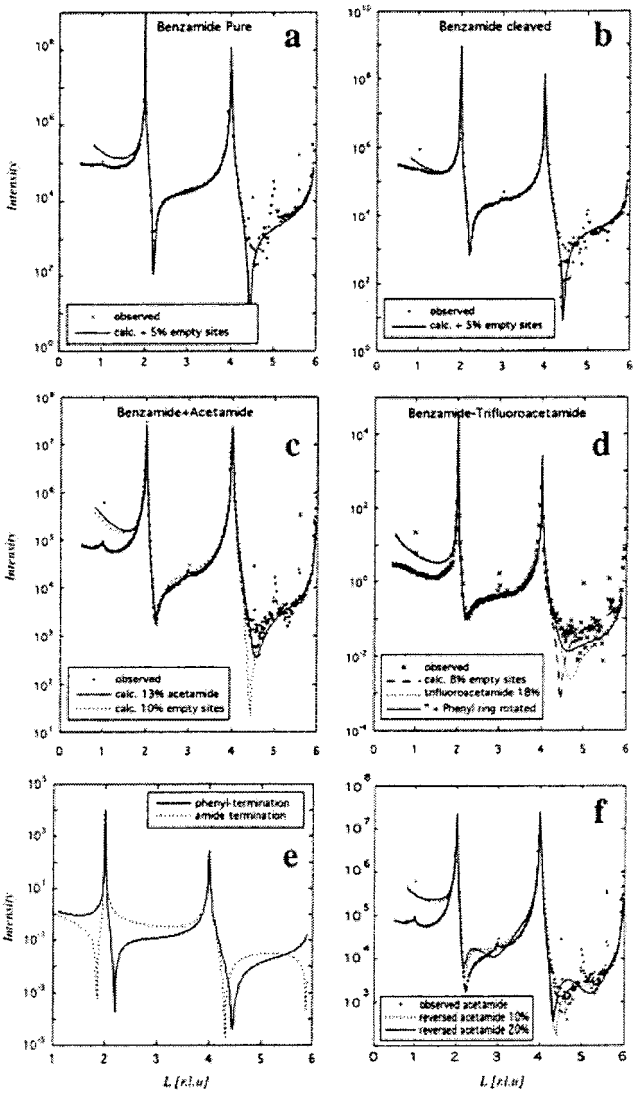

Figure 5. Observed (×) and calculated (—) (00*l*) crystal truncation rods for pure and affected benzamide crystals. (a) Pure crystal, surface modeled by layer containing 5% empty sites. (b) Cleaved surface of a pure crystal. (c) Cleaved surface of a pure crystal grown from a 1:1 benzamide−acetamide mixture. The model surface layer contains either 13% acetamide or 10% empty sites. (d) Cleaved surface of a pure crystal grown with 1:1 benzamide−trifluoroacetamide. The model surface layer contains either 8% empty sites (- - -) or 18% trifluoroacetamide (···). Improvement to the calculated model is achieved with rotation of the phenyl rings (—). (e) Calculated intensity profile for a model terminated by amide groups or phenyl groups. (f) Calculated intensity profiles for a structure in which the acetamide moiety is incorporated into the second layer with the $-CH_3$ group pointing toward the bulk. (Reprinted with permission from ref 12. Copyright 1999 American Chemical Society.)

distinctly different in the regions $l \approx 2.2$ and 4.5, pointing to a systematic difference in the surface structure. The intensity profile in Figure 5c was fitted by two possible surface layer models, with or without acetamide molecules. The first model was composed of benzamide sites and empty sites in a 90:10 occupancy ratio (dashed line in Figure 5c); the second model was composed of benzamide and acetamide sites in a 87:13 occupancy ratio (solid line). The latter model clearly fits the measured CTR data better. The

(00*l*) intensity profile of a benzamide crystal grown from a trifluoroacetamide−alcohol solvent mixture (Figure 5d) was also significantly different from that of pure benzamide in the region $l = 4-6$, fitting a model with a 82:18 occupancy ratio.

It is important to note that the calculated intensity profiles are extremely sensitive to variations in the surface model, and alternative models (e.g., ones with the CH_3 and CF_3 moieties of the amide cosolvent incorporated into the second layer facing into the bulk) fit the data poorly (Figure 5f). This indicates that the amide cosolvents are not incorporated with the CF_3 or CH_3 groups in contact with the underlying layer of the bulk.

Other GIXD studies have emerged that further demonstrate the structural relationships between 2-D Langmuir monolayer structures and 3-D crystals.[13,14] For example, the two-dimensional crystal packing arrangements of enantiomerically pure and racemic α-amino acid $RCH(NH_3^+)CO_2^-$ monolayers on water and on aqueous solutions containing glycine were examined by GIXD.[15] The amphiphiles were designed so that their racemic mixtures form with heterochiral two-dimensional crystals (for $R = C_nH_{2n+1}$, $n = 10, 12, 16$) due to the tendency for herringbone chain arrangements via glide symmetry or homochiral two-dimensional crystals (for $R = C_nH_{2n+1}CONH(CH_2)_4$, $n = 11, 17, 21$) by hydrogen-bonding enforced interchain translation of the amide group that leads to spontaneous segregation into islands of opposite chirality. GIXD revealed a correlation between the packing arrangements of these two-dimensional crystals and the orientation α-glycine crystals nucleated by these monolayers. The correspondence between 2-D Lamgmuir monolayers and 3-D crystals has been illustrated further with a detailed description of the phase behavior of Langmuir monolayers and bulk alkane crystals.[16]

The formation of oriented crystalline monolayers of a 2×2 square grid complex of Ag(I) ions and 3,6-bis[2-(6-phenylpyridine)]pyridazine was formed by spreading the water-insoluble ligand on the upper surface of an aqueous subphase containing dissolved Ag(I).[17] Synchrotron grazing-incidence X-ray diffraction and specular X-ray reflectivity, coupled with structural refinement that enabled detection of the positions of the counterions, confirmend the existence of the 2×2 square grid complex. Scanning force microscopy of the monolayers (see following section), after transfer from the air−water interface onto various solid supports, revealed a monolayer thickness of 14 Å, consistent with the structure deduced by X-ray scattering. Interestingly, surface compression of the initial self-assembled monolayer induced a transition to a crystalline *bilayer* in which the structure of the two layers was nearly identical to their original arrangement. Furthermore, the two layers were in registry. This example illustrates that X-ray diffraction and scanning probe microscopy are a powerful combination that not only provides detailed insight into structure, but also into processes that are relevant to crystal nucleation.

2. Scanning Probe Microscopy of Crystal Surfaces

Most techniques employed for characterization of organic crystal surfaces at the near-molecular level are performed ex situ, requiring characterization after formation of the crystal surface or after a chemical process has occurred at a crystal surface. For example, numerous articles have appeared over the last five years that describe the use of scanning tunneling microscopy[18−23] in characterization of organic crystal surfaces, although this method is limited to electrically conductive samples. Consequently, these studies have involved primarily low-dimensional organic conductors consisting of electron donors and acceptors such as tetrathiafulvalene, tetracyanoquinodimethane, and related compounds. STM is capable of measuring lattice parameters of the imaged face and estimating heights of steps separating individual crystal planes on these faces. In this respect, STM provides crystallographic structural information in the form of three lattice constants. However, caution needs to be exercised as STM data actually probes the density of states near the Fermi level, which may not exhibit a one-to-one correspondence to the crystallographic structure.

Given that most crystal materials are poor electrical conductors, atomic force microscopy (AFM) is emerging as the method of choice for characterizing the surface structure of crystals. The AFM, reduced to practice in 1986 by Binnig, Quate, and Gerber,[24] operates much like a surface profilometer. A small tip, usually silicon or silicon nitride, at the end of a silicon cantilever is moved in small increments with piezoelectric actuators over the sample (or the sample is moved under the tip) while in contact with the sample surface. A two-dimensional image is acquired by rastering the tip over a specified area of the sample. Imaging can be accomplished at constant force, in which the tip traces the nominal topography of the surface. Alternatively, data can be collected in constant height mode, in which the tip is kept at a constant height above the sample and the force between the tip and sample measured. The force between the sample and tip is deduced from the position of a laser beam, reflected off the back of the cantilever, on a spatially sensitive photodiode detector (Figure 6). When the tip experiences an attractive force, the cantilever bends toward the sample so that the laser position on the detector moves downward. Conversely, a repulsive interaction causes the cantilever to bend away from the sample so that the laser position moves upward. The deflection of the tip is calculated from the laser spot intensity from quadrants (A+B)−(C+D).

Measurement of the actual force requires determination of the cantilever force constant. Approximate values of the force constant are generally provided with commercially available cantilevers. However, precise force measurements require determination of the force constant by more exact methods.[25] The applied force is given by Hooke's law, $F = -k\Delta z$, where k is the force constant of the cantilever and Δz is the cantilever displacement. The "force curve" in Figure 7 illustrates the behavior of the tip as it approaches and engages a typical sample and then

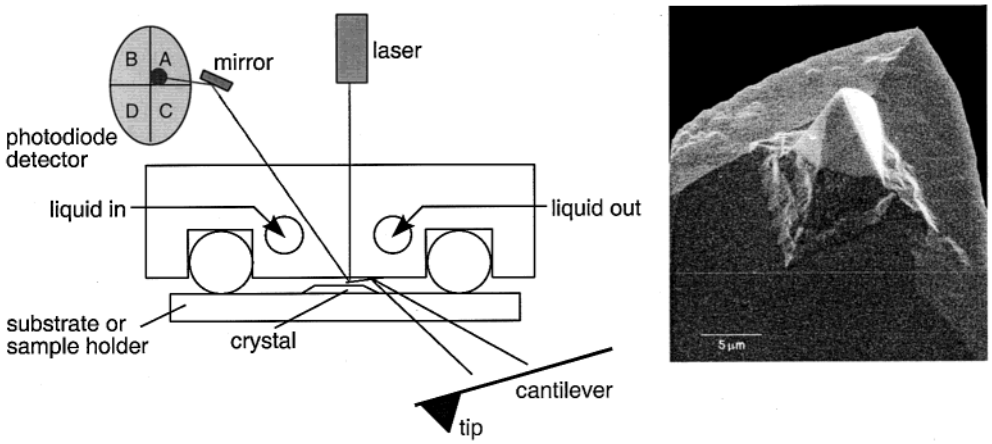

Figure 6. (left) Schematic of atomic force microscopy detection method. A laser is reflected off of the cantilever and detected with a four-segment detector. This allows visualization of both topographical and frictional information. (right) Scanning electron micrograph of a pyramidal Si_3N_4 AFM tip at the end of a silicon cantilever.

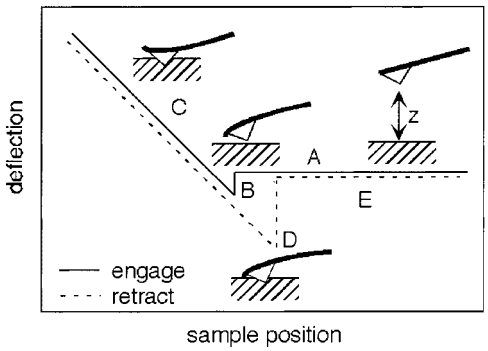

Figure 7. Schematic of a typical force curve observed with the AFM. (A) Tip and cantilever approach sample surface, (B) jump-to-contact due to attractive forces, (C) repulsion of the tip, (D) disengagement or "pull-off, (E) tip completely disengaged from surface.

retracts. In region "A" the tip and cantilever approach the sample surface until at "B" the tip "jumps to contact". This event occurs when the gradient of the force with respect to distance z ($\Delta F/\Delta z$) exceeds the force constant of the cantilever, thereby causing the cantilever to "jump" toward the sample and the laser beam to move downward on the detector. Further advancement of the tip toward the sample results in repulsive interactions in region "C". This forces the cantilever to bend in the opposite direction so that the laser beam moves upward on the detector. During retraction the process reverses but the tip remains engaged beyond the jump-to-contact distance and the force required for disengagement at "D", commonly referred to as the "pull-off" force, exceeds that observed at jump-to-contact. Eventually the tip completely disengages to zero force in region "E". The hysteresis of the force curve is due to adhesive forces that result from penetration of the sample by the tip during the repulsive excursion.

Two imaging modes are possible with conventional "contact mode" AFM. In constant height mode, the force changes experienced by the tip are deduced from changes in the deflection of the cantilever. In constant force mode, a feedback loop is used to maintain a constant cantilever deflection by adjusting the height of the cantilever relative to the sample as the tip traces the topography of the surface surface. This mode provides a topographic profile of the surface with a vertical resolution approaching 0.1 Å, although any height differences deduced from the data assume that the tip−sample interaction is identical. This may not be a safe assumption when comparing regions of a sample with different surface compositions. The true lateral resolution is limited by the radius of curvature of the tip, which for conventional AFM tips has values exceeding 15 nm.

A key issue for imaging of organic crystal surfaces is the susceptibility to mechanical damage as the AFM tip is rastered across the surface in the contact mode. Forces in excess of of 10^{-11} N are sufficient to cause mechanical damage on soft organic crystal surfaces. This is problematic when imaging in air or vacuum, where the van der Waals interaction is strongly attractive and the tip strongly engages the sample. Mechanical damage is exacerbated in air by capillary forces between the tip and sample that result from capillary condensation of water between the closely spaced tip and sample. Under these conditions, etching of the sample surface as the tip is rastered is quite common.

Fortunately, performing AFM in solution eliminates capillary forces while, for suitable fluids, it reduces tip−sample forces. In general terms, the van der Waals energy between two objects is given by $w(r) = -Cr^{-6}$, where C is a constant (in units of J m^6) with a magnitude proportional to the attractive interaction between the two objects. Laws describing the interactions between two objects of various geometries can be devised by integrating the energies of all the atoms in one object with all the atoms in the other to derive a "two-body" potential that can be described in terms of the Hamaker constant, A, which is given by $A = \pi^2 C \rho_1 \rho_2$, where ρ_1 and ρ_2 are number densities (in units of m^{-3}).[26,27] In the case of a sphere (i.e., the AFM tip) interacting with a planar surface (i.e., a flat sample), the interaction energy between the tip and the sample can be approximated as $W = -AR/6D$, where R is the radius of curvature of the tip and D is the tip−sample separation. The Hamaker constant for materials 1 and 2 interacting across medium 3,

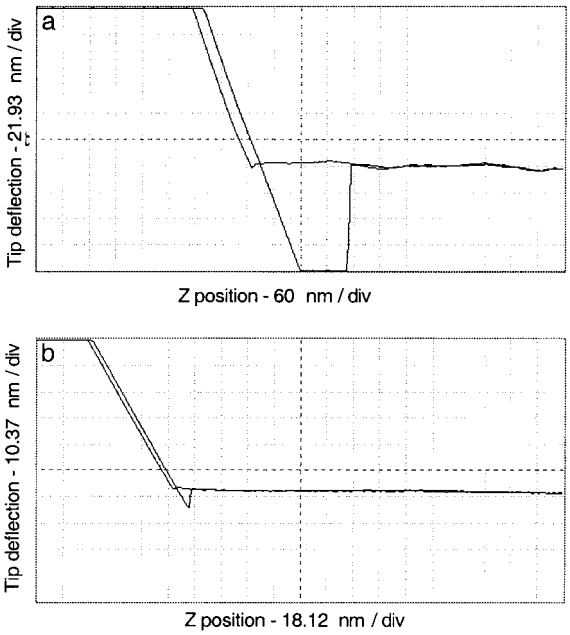

Figure 8. Force curves obtained with AFM on a HOPG substrate (a) in air and (b) in ethanol, illustrating the reduced jump-to-contact and pull-off forcees when imaging in a fluid.

obtained from a modified form of the Lifshitz theory, is given by eq 1[26,28]

$$A = \frac{3kT}{4}\left(\frac{\epsilon_1 - \epsilon_3}{\epsilon_1 + \epsilon_3}\right)\left(\frac{\epsilon_2 - \epsilon_3}{\epsilon_2 + \epsilon_3}\right) + \frac{3h\omega}{8\sqrt{2}}\left[\frac{(n_1^2 - n_3^2)(n_2^2 - n_3^2)}{(n_1^2 + n_3^2)^{1/2}(n_2^2 + n_3^2)^{1/2}[(n_1^2 + n_3^2)^{1/2} + (n_2^2 + n_3^2)^{1/2}]}\right] \quad (1)$$

where A_{132} is the Hamaker constant between the tip (1) and sample (2) in the liquid medium (3), ϵ_i and n_i are the dielectric constant and refractive index of medium I, and $h\omega$ is ground-state oscillation energy of the electron. For example, the Hamaker constant for the (tip)Si_3N_4|air|HOPG(sample) is 1.2×10^{-19} J, whereas for (tip)Si_3N_4|ethanol|HOPG(sample) $A = 9.0 \times 10^{-20}$ J, indicating a decrease in the tip−sample interaction in the presence of ethanol (HOPG = highly oriented pyrolytic graphite).[29] Force curves obtained for these two configurations clearly demonstrate the role of the fluid, with reduced jump-to-contact forces and reduced pull-off forces that are indicative of the reduced tip−sample interactions (Figure 8). The reduced interaction and the absence of capillary forces conspire to reduce mechanical etching of soft samples.

Another consequence of the imaging in fluids is an improvement in lateral resolution. The resolution scale of AFM, RS, determined by the area of contact between the tip and the sample, is described by eq 2,[30] where R_0 and D_0 are the AFM tip radius and the minimum tip−surface separation allowed by repulsive contact forces, respectively, K is the combined elastic modulus of the tip and sample, and A_{132} is the Hamaker constant. According this equation, AFM resolution decreases with increasing van der Waals attraction between the tip and the sample.

$$\mathrm{RS} = \left(\frac{A_{132}R_0^2}{8KD_0^2}\right)^{1/3} \quad (2)$$

It is important to note that the imaging mechanism does not involve contact of the sample with a single atom on the tip. In fact, if this were the case, the pressure exerted on the sample with the typical force of 10^{-10} N would be approximately 10^{-10} N/10^{-18} m^2. This stress, equivalent to 100 MPa, is approaching the tensile strengths of most metals and is clearly unrealistic given the observed mechanical stability of many materials during AFM imaging. Rather, the total force between the tip and sample, being macroscopic bodies, is determined by integrating the interatomic forces over the volume of the tip and the sample. The interaction force between a macroscopic tip and surface actually is rather long range, scaling as D^{-2}, where D is the tip−sample separation. This increases the effective contact area of the tip, thereby limiting the resolution to the radius of curvature of the tip, which typically has values of approximately 30 and 15 nm for conventional Si_3N_4 and Si tips, respectively. Because the force is distributed over a larger contact area, the mechanical stress on the surface is significantly reduced so that imaging is feasible.

This resolution limit seems to contradict the numerous AFM images that have been reported in which atomic- or molecular-scale periodicities are observed. Interestingly, atomic or molecular contrast is almost always limited to ordered crystalline samples which have large atomically (or molecularly) flat single-domain areas. In the late 1980s, shortly after AFM became widely available, atomic contrast was commonly observed on layered materials such as graphite and metal chalcogenides, which tended to have large atomically smooth layer faces. This prompted a rather reasonable suggestion that the atomic contrast was due to the periodic forces between the sample surface and a "flake" of the sample picked up by the tip in a previous scan.[31] However, numerous recent studies have illustrated that molecular-scale contrast can be obtained for molecular crystals, which cannot form intact flakes having the structural integrity required for such an imaging mechanism. This argues that atomic- or molecular-scale contrast is simply due to the periodic forces felt by the tip as it moves over the surface of the periodic lattice of the sample, generating what is tantamount to a Moiré pattern of the convolved forces between the macroscopic tip and periodic lattice of the sample. This is akin to rolling a bowling ball over an ordered array of small ball bearings—the bowling ball still "feels" the repetitive contour of the sample surface even though it is much larger than the period of the surface. Fortunately, the layered nature of many organic crystals leads to exposed crystal planes with sufficiently large areas to allow attainment of molecular-scale contrast. However, it must be emphasized that molecular-scale *contrast* is not identical to molecular-scale *resolution*.

The four-segment diode detector also allows measurement of cantilever "twist" that can result from frictional interactions with the sample surface. The

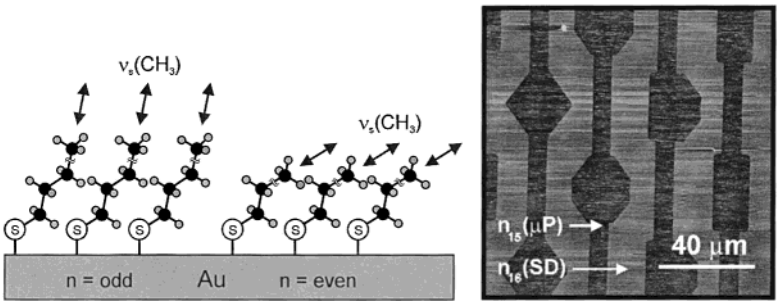

Figure 9. (left) Idealized structures for *n*-alkanethiolate monolayers chemisorbed on gold. The value of *n* refers to the number of methylene groups in the alkyl chain. (right) Friction image (120 μm × 120 μm) of patterned alkane thiols on smooth gold substrates. In this example the pattern is fabricated by microcontact printing regions of $CH_3(CH_2)_{15}SH$ and then depositing $CH_3(CH_2)_{16}SH$ directly from solution. The brighter contrast in the $CH_3(CH_2)_{16}SH$ regions corresponds to higher friction. (Reprinted with permission from ref 37. Copyright 1998 American Chemical Society.)

magnitude of the friction will dictate the degree of twist exhibited by the cantilever. Friction information is typically collected with the scan direction perpendicular to the long axis of the cantilever, although cantilever twist can also occur when the scan direction is parallel to the length of the cantilever because the tip has an irregular, not hemispherical, shape. This image mode—referred to as friction force microscopy (FFM) or lateral force microscopy (LFM)—produces a friction map of the substrate surface from the laser intensity measured from quadrants (A+C)−(B+D). LFM has been used to image phase separation in LB films,[32] the surface of polymer and copolymer films,[33,34] domains of an organic bilayer with different friction due to different 2-D orientations,[35] and domains of a crystalline organic monolayer with different friction due to different 2-D orientations.[36] This can be illustrated by lateral force images obtained on gold surfaces patterned with monolayers of two different alkanethiol monolayers that differed in length, one having an odd number of carbon atoms and the other an even number.[37] The monolayer patterns can be fabricated by "microcontact printing" one alkane thiol followed by deposition of the second one from solution. The AFM images reveal substantial lateral force contrast between the different regions that can be attributed to the different orientations of the methyl groups at the monolayer surface (Figure 9).

An increasingly popular AFM imaging mode that is being used increasingly to examine soft materials is the "tapping mode," in which the cantilever is actually vibrated at a specific frequency (in fluids, this frequency typically has values of 15−20 kHz) so that the tip only makes intermittent contact with the sample surface. This has the benefit of reducing mechanical damage but carries a penalty of reduced resolution as the average tip−sample separation is larger than in contact mode.

The ability to image crystals with molecular-scale contrast enables determination of the lattice parameters of the imaged plane, while step heights can provide the lattice constant normal to the plane. If molecular-level contrast can be achieved on two successive terraces in a single image frame, the registry of overlapping terrace planes can be determined, making it possible to deduce possible space groups. Consequently, AFM can be useful for identification or confirmation of crystal structure. Lattice images of crystal surfaces have been obtained for numerous organic crystals in air and in fluid media, including organic conductors[38,] (which also have been investigated by STM[9−14]), organic dyes,[39] amino acids,[40] various proteins,[41,42,43] and even the satellite tobacco mosaic virus.[44] If the crystal surface under examination is a low-energy surface, the lattice parameters obtained from AFM data generally are consistent with those expected based on bulk crystallography. Studies of numerous organic crystals in our laboratory have indicated that AFM and crystallographic dimensions will typically differ by <5%. These differences may be attributed partially to measurement error inherent in the AFM, although surface reconstruction with concomitant reduction in surface energy is also likely. Much of these data are acquired in liquids, so reconstruction can also result from surface interaction with solvent molecules.

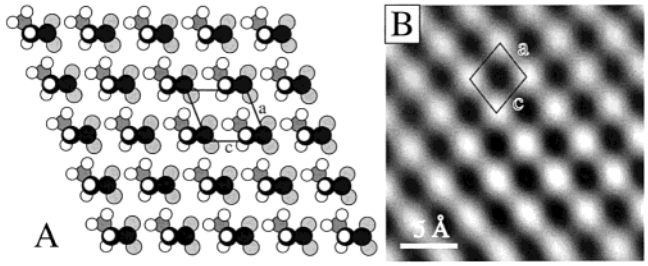

Figure 10. (A) Model of the (010) plane of glycine and (B) AFM image of the (010) surface of a glycine crystal acquired in an aqueous solution saturated with glycine. The monoclinic cell drawn on both figures is of identical dimensions.

The capabilities of AFM for lattice imaging of single crystals can be illustrated by several examples. The prominent face of a single crystal of glycine consists of the (010) plane, as expected from the prominent two-dimensional hydrogen-bonded layers in this plane. Lattice images obtained on this crystal face exhibit symmetry and periodicity identical to that of the (010) plane (Figure 10).

AFM images obtained recently in our laboratory of the monoclinic photographic dye *N*-[4-[4-cyano-2-(2-furanylmethylene)-2,5-dihydro-5-oxo-3-furanyl]-phenyl]-1-butanesulfonamide (**1**) indicated a rectangular unit cell with dimensions of 20.1 and 8.2 Å, which compare favorably to the crystallographic values for the (100) plane of b = 18.908 Å and c =

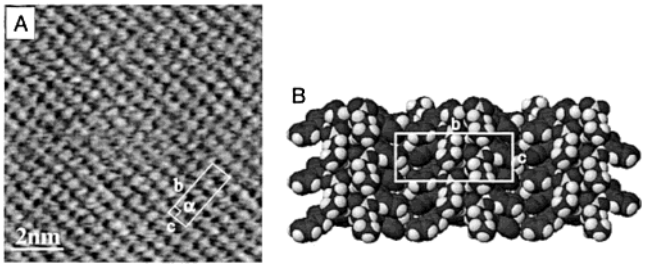

Figure 11. (a) Lattice image obtained for the (100) plane of *N*-[4-[4-cyano-2-(2-furanylmethylene)-2,5-dihydro-5-oxo-3-furanyl]phenyl]-1-butanesulfonamide (**1**) obtained in 2-propanol. The rectangular unit cell represents the periodicity surmised from the real space and Fourier transform of the data. (b) A space-filling view of the (100) plane.

7.904 Å (Figure 11). The step height measured from the AFM data was 13.0 Å, identical to the value of the third lattice parameter, $a = 12.972$ Å. In both cases, the lattice images were acquired under conditions in which the single crystals were actually growing (vide infra).

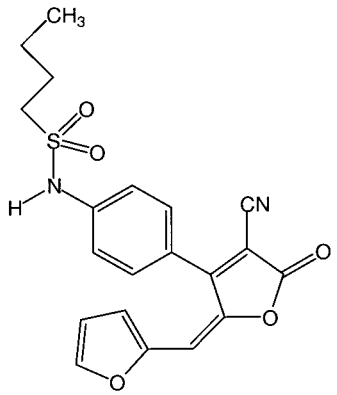

1

Molecular lattice images of the therapeutically important protein insulin, obtained in our laboratory, can provide important structural information for crystals that are not amenable to characterization by X-ray diffraction. Insulin crystals are extremely soft, requiring the use of tapping mode rather than the conventional contact mode. Direct acquisition of lattice images enables rapid identification of polymorphs formed under different crystallization conditions directly in the AFM cell. For example, the (001) plane of the *R*6 *rhombohedral* polymorph exhibits contrast with hexagonal symmetry and a lattice parameter of 42.8 ± 6.4 Å, in agreement with the expected value of 45.65 Å from single-crystal X-ray diffraction. In contrast, the (001) plane of the *R*6 *monoclinic* polymorph exhibited a rectangular lattice with $a \approx b = 45.8 \pm 1.0$ Å, in good agreement with the nearest-neighbor contacts in the (001) plane (Figure 12). In both cases these surface planes consist of layers of insulin hexamers, which produce 43−50 Å step heights separating overlapping terraces, equivalent to the *c* lattice constant of both forms. Imaging of successive terraces enables determination of the registry of contacting planes, providing further confirmation of the space groups of these polymorphs.

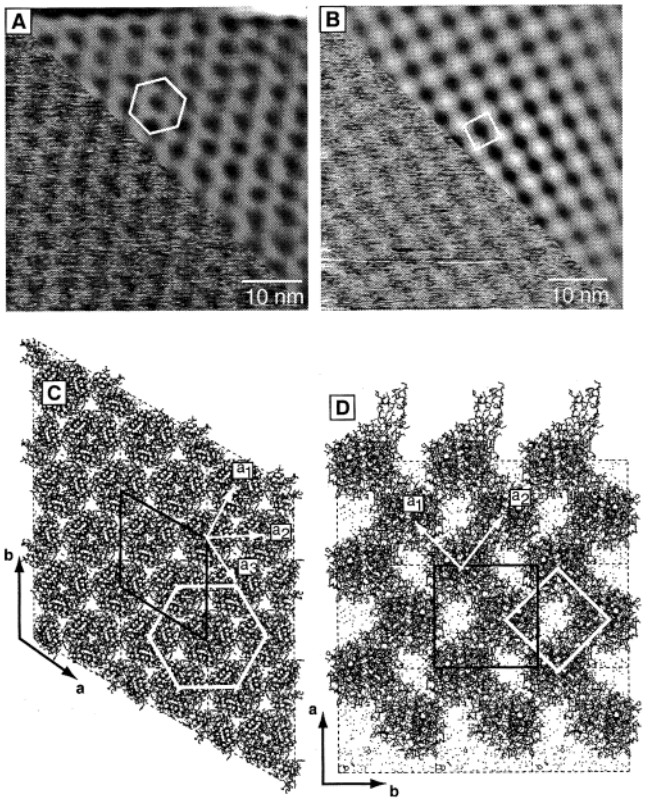

Figure 12. Atomic force microscopy of the (A) rhombohedral R6 and the (B) monoclinic R6 polymorphs of bovine insulin. The lower left half of each image represents the raw data acquired with tapping-mode AFM, while the upper left half represents Fourier-filtered data. The structures of the (001) planes of the two forms are illustrated in C and D below their respective AFM images. (Reprinted with permission from ref 41. Copyright 1996.)

AFM tapping mode can also be employed to image more than one face of a single crystal, as illustrated here for bovine insulin (Figure 13). This allows lattice imaging of adjoining crystallographic planes, thereby enabling morphology characterization of very small crystals and verification of space group symmetry.

III. Molecular Organization on Crystal Surfaces

A. Homoepitaxial Crystal Growth

Crystal growth, in which incoming solute molecules attach to the surface of an existing crystal plane of the same material, can be described as a "homoepitaxial" process. The term "epitaxy" derives from the Greek roots "*επι-*" meaning "upon" and "*ταξι-*" meaning "order." It was most likely used as a military term to describe orderly rows of soldiers in a parade upon a battlefield, not unlike the process of building a crystal by arranging molecules layer-by-layer.[45] The modern definition of this term is the lattice registry between two opposing lattice planes, each plane consisting of ordered arrays of molecules. Of course, during crystallization of a single phase, this registry is essentially perfect as the incoming solute molecules arrange as layers identical to the crystal plane upon which growth is occurring.

At first glance crystal growth may mistakenly be perceived as trivial. However, it is actually a rather

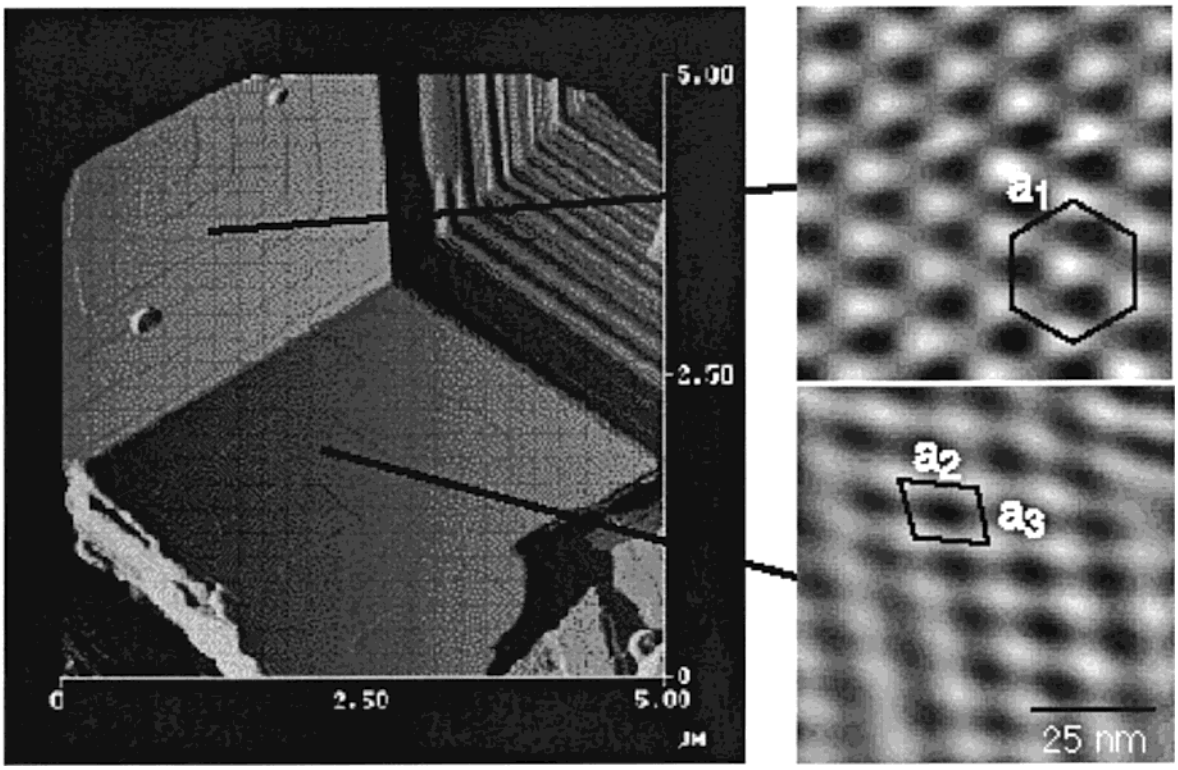

Figure 13. (left) In situ AFM tapping-mode image acquired across the intersection of three crystal faces of a bovine insulin crystal. Scan size = 5 μm × 5 μm. Well-defined screw dislocations, from which the terraces emanate, are evident. (right) Lattice images acquired on two different crystal planes of the insulin crystal. The upper image can be assigned to the (001) plane (AFM: $a_1 = 43 \pm 4$ Å; $\gamma = 62° \pm 4°$; crystal structure: 46 Å; $\gamma = 60°$), while the lower image can be assigned to the (110) plane (AFM: $a_2 = 33.5 \pm 3$ Å; $a_3 = 45.1 \pm 4$ Å; $\gamma = 60° \pm 3°$; crystal structure: $a_1 = 37.8$ Å; $a_2 = 47.7$ Å; $\gamma = 61°$). (Reprinted with permission from ref 64h. Copyright 1998.)

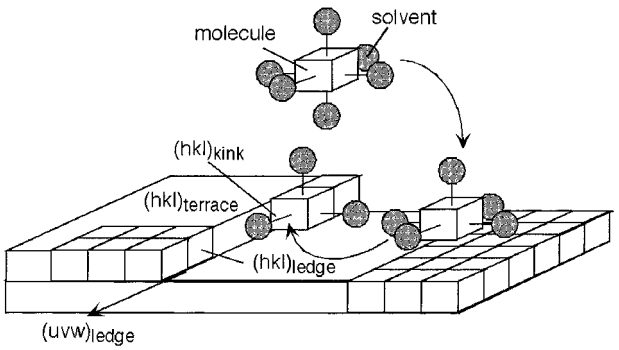

Figure 14. Schematic representation of the terrace–ledge–kink model for crystal growth.

complex process that involves solute molecules shedding solvent molecules and attaching to a specific crystal plane in the proper orientation, diffusion along the surface to other attachment sites, and attachment in the proper orientation. The most accepted model for crystal growth is the terrace–ledge–kink (TLK) model (Figure 14) in which a crystal surface is described as having a large terrace decorated by ledges, which are defined by a crystallographic direction along the intersection of the terrace plane and a specific step plane. The ledge is decorated with "kinks" that result from the attachment of solute molecules to the ledge, forming a third crystallographic plane that intersects the step plane. The relative proportions of these features are governed by their surface energies, their interaction with solvent molecules, additives or impurities, and the excess free energy at the interface. The latter depends on factors such as temperature and solute concentration. By inference from their relative areas, the surface energies of these topographical features decrease in the order $\gamma_{terrace} > \gamma_{ledge} > \gamma_{kink}$.

While the TLK model had been devised as a universal description for crystal growth, it has generally been applied and verified for simple inorganic systems (e.g., silicon) based on ex situ observations. However, several laboratories in the past decade have investigated crystal growth of more complex inorganic and organic materials with AFM, obtaining direct visualization of growth processes in situ and in real time. AFM can also provide insight into dissolution processes, the microscopic reverse of growth. In a recent investigation, the crystal dissolution of KBr crystals was imaged *and controlled locally* by an AFM tip.[46] This was accomplished by applying a potential to a metal-coated AFM tip so that bromide ions in solution were oxidized in the region between the tip and the KBr crystal surface. The resulting reduction in bromide concentration created local undersaturation at the crystal surface, instigating crystal dissolution that could be imaged simultaneously with the tip.

Direct visualization of growth processes are nicely illustrated by AFM studies, in aqueous media, of potassium dihydrogen phosphate,[47] which is of interest because of the nonlinear optical properties of this material, and calcite growth, which has attracted

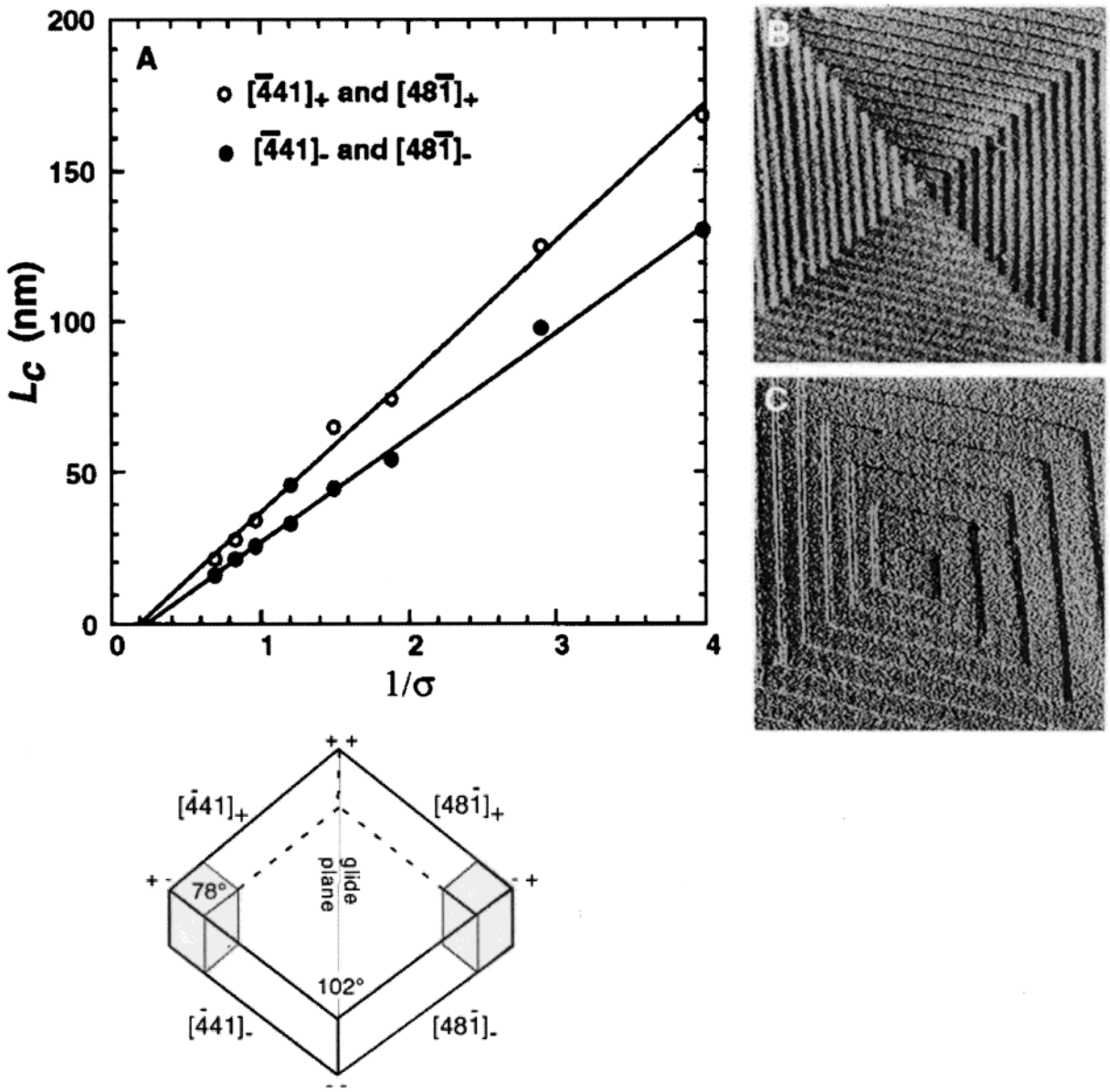

Figure 15. (A) Dependence of critical length on supersaturation along with images (5 × 5 μm) showing effect of Lc on T±: (B) high, short Lc; (C) low, long Lc. (D) Schematic of a calcite {104} terrace illustrating anisotropy, step directions, and glide plane. (Reprinted with permission from ref 49. Copyright 1998 American Association for the Advancement of Science.)

interest because of its relevance to biomineralization.[48] At the time of this writing, one of the more thorough in situ AFM studies of calcite crystal growth was reported by Teng et al.,[49] who examined calcite crystallization on a seed crystal in a solution of fixed ionic strength and pH. These experiments were performed by continuously passing a supersaturated solution through an AFM fluid cell at rates so that step velocity was independent of flow rate and growth was not limited by mass transport to the surface. Crystal growth occurred on {10$\bar{1}$4} faces by the generation of new steps from dislocations. The dynamic capabilities of AFM enabled measurement step lengths immediately before and after the onset of their advancement so that step velocity could be determined as well as the average step length, L_c.[50] The supersaturation, σ, is defined by $\sigma = \Delta\mu/k_bT$, where $\Delta\mu$ is change in chemical potential per molecule, k_b is Boltzmann's constant, and T is absolute temperature. For calcium carbonate in solution, the supersaturation could be determined by $\sigma = \ln[a(Ca^{2+})a(CO_3^{2-})]/K_{sp}$, where $a(i)$ is the activity of the ith species and K_{sp} is the equilibrium solubility at zero ionic strength (estimated as $10^{-8.54}$). For σ = 0.04−1.4, layer growth of calcite occurred on {10$\bar{1}$4} faces by advancement of 3.1 Å monomolecular steps generated from dislocations and separated by atomically flat {10$\bar{1}$4} terraces (Figure 15). Step advancement results in the formation of polygonal growth hillocks with steps parallel to ⟨$\bar{4}$41⟩ directions, the *c*-glide symmetry plane generating two distinct pairs of crystallographically identical steps that were denoted as positive ([$\bar{4}$41]+ and [48$\bar{1}$]+) and negative ([$\bar{4}$41] and [48$\bar{1}$]) directions.[51]

The thermodynamics of step advancement were deduced from measured terrace widths $T_\pm$ and step speeds $v_\pm$, related by $T_+/T_- = v_+/v_-$. The total growth rate of the crystal normal to the surface, R, was determined by $R = hv_\pm/T_\pm$, where h is step height. The values of $v_\pm$, reflecting the attachment and

detachment kinetics at kink sites on the steps, differed for the two step types because of nonequivalence in kink site structure.

If a new spiral segment remains in equilibrium with the adjacent reservoir of solute growth units, then it will advance only when the change in free energy, Δg, associated with the addition of a new row of growth units, organized parallel to the step, is negative. Taking into account the anisotropy in calcite step structure, Δg for a straight step is given by eq 3

$$\Delta g_{\pm} = -(L/b)\Delta\mu + 2c\langle\gamma\rangle_{\pm} \quad (3)$$

where

$$\langle\gamma\rangle_{+} = {}^{1}/_{4}[2(\gamma_{+} + \gamma_{-}) + (\gamma_{++} + \gamma_{+-})$$

$$\langle\gamma\rangle_{-} = {}^{1}/_{4}[2(\gamma_{+} + \gamma_{-}) + (\gamma_{--} + \gamma_{+-})$$

and L is the length of the step, b is the 6.4 Å intermolecular distance along the step, c is the 3.2 Å distance between rows, γ_{+} and γ_{-} are the step edge free energies along the + and − steps, and γ_{++}, γ_{--}, and γ_{+-} are contributions to the step edge free energy from the corner sites. If Δg is set to zero and appropriate substitutions are made, it can be shown that steps advance only if L exceeds a critical value, L_c, given by eq 4. As mentioned above, L_c was surmised experimentally from the average of the lengths of the steps before and after they began to advance. The inverse relationship between L_c and σ in eq 4 is predicted by the Gibbs−Thomson effect, which applies to systems under thermodynamic control.[52]

$$L_{c\pm} = 2bc\langle\gamma\rangle_{\pm}/k_bT\sigma \quad (4)$$

The authors of this work indeed demonstrated that the measured L_c varied inversely with σ for both step directions on the calcite {10$\bar{1}$4} faces (Figure 15), the slope of $L_c - 1/\sigma$ plots giving values of $\langle\gamma\rangle_{+} = 2.75$ and $\langle\gamma\rangle_{-} = 2.15$ eV/nm. Consequently the difference between $\langle\gamma\rangle_{+}$ and $\langle\gamma\rangle_{-}$ associated with the ++ and − − corners was approximately 0.77 eV per molecule. The linearity of the $L_c - 1/\sigma$ plots *demonstrated that the observed crystal growth mode was governed by equilibrium thermodynamics*. This may seem surprising because attachment and detachment kinetics will be controlled by local atomic configurations at kink sites along the steps and sites far from the corners should exhibit local dynamics that are independent of step length. When $\sigma > 1$, attachment to these high-energy sites will always be more rapid than detachment, even on a subcritical step. The observation of linear $L_c - 1/\sigma$ data indicated that growth was governed by equilibrium with the crystallization medium even at the sites of high curvature near corners where detachment is preferred. That is, sites along the step must communicate with the near-corner sites on a time scale that is short compared with the time required to add another row. These results imply that transport along the steps and addition of rows of solute molecules was rapid enough to keep steps in equilibrium with the adjacent fluid. The data obtained by AFM also enabled determination, from the nonzero intercept $L_c - 1/\sigma$ plots, of the value of $\sigma_{\pm}$ where $L_{c\pm}$ reaches zero, which defines the condition under which the steps will become kinetically roughened. This enabled a rough determination of the free energy barriers for one-dimensional nucleation at the steps, $\Delta g_{1D\pm}$, yielding values of $\Delta g_{1D+} = 0.14$ eV and $\Delta g_{1D-} = 0.10$ eV.

The effects of molecular additives on bulk crystal morphology are typically thought to stem from attachment of the additive to the crystal plane of an actively growing face, producing a defect that acts either as a "blocker" (if the additive adsorbs on or is incorporated into the crystal plane so that it protrudes from the interface) or as a "disruptor" (if it is incorporated into the crystal plane so as to leave a pseudo-vacancy). Growth inhibition at individual steps results in each case from a reduction in Δg upon addition of the next row of molecules. The specific molecular recognition events responsible for this effect, which has been investigated for various amino acids[53] and reviewed recently,[54,55] generally can be deduced from the bulk morphology of the crystals and comparison to the 3-D crystal structure. This concept has even been extended to antibody recognition and cell adhesion on specific crystal planes of protein crystals.[56−60] Specific molecular recognition is also suggested in recent studies of the influence of molecular additives, or "auxiliaries", on glycine polymorphism.[61] In this case, polymorph selectivity is most likely governed by the binding preference of a molecular additive for a crystal plane, or set of planes, of a particular polymorph. The selective attachment of the auxiliary to the surface of a polymorph will prevent further growth of that polymorph. In contrast, growth of unperturbed polymorphs will not be impeded, and these phases will eventually precipitate. This concept is similar to earlier work in which chiral auxiliaries were used to resolve enantiomers by crystallization.[62] The growth of α,ω-docosanediol into 3-D crystallites can be inhibited by amphiphilic additives [63] Whereas the specific recognition events responsible for these effects have been surmised from the changes in crystal morphology and comparison to the 3-D crystal structure of a selected material, the ability of AFM to probe crystal topography in situ and in real time enables (i) elucidation of these events at the near-molecular scale, (ii) acquisition of lattice images so that terraces, ledges, and kinks influenced by additives can be assigned to specific crystallographic planes, (iii) measurement of growth rates, terrace widths, dislocation curvature, and defect structures, providing kinetic as well as thermodynamic data reflecting these recognition events at the crystal surface.

These capabilities can be illustrated by the influence of aspartic acid on calcite growth. Addition of aspartic acid to growth solutions has a dramatic effect on the spiral morphology, with the hillocks becoming asymmetric and rounded, signifying new step directions, and a change in the terrace widths (Figure 16). The step rounding can be partially attributed to kinetic factors, but the presence of new

Figure 16. AFM images (9 × 9 μm) showing effect of aspartic acid on growth hillock morphology before (A) and after (B) addition. Solid vertical lines show location of glide plane. (Reprinted with permission from ref 49. Copyright 1998 American Association for the Advancement of Science.)

equilibrium step directions indicates a change in the energies of the crystal facets. The much smaller terrace widths and therefore an increase in the number of steps are consistent with a lower step edge free energy, estimated to be approximately 1 eV per molecule. This value, which was smaller than for steps on pure calcite by a factor of about three, suggests that aspartic acid forms adsorbs readily on the new step directions and lowers their surface free energy.

AFM investigations in our laboratory revealed that additives influence crystal growth modes for organic crystals as well. During crystal growth, the organic crystalline dye **1** (depicted in Figure 11) exhibits prominent (100) faces decorated with 13 Å high monomolecular steps separating molecularly flat (100) terraces (Figure 17). Lattice images (see Figure 11) obtained by scanning over a small area of the terrace indicated that the steps were oriented along the [010] direction. On the basis of inspection of the structure, the step plane could be assigned to (010). Addition of the anionic octylphenyl oligoether sulfate **2** to the crystal growth medium resulted in a drastic change in (100) surface, with the steps becoming highly "curved" and the terrace widths decreasing substantially. This behavior can be explained by adsorption of the surfactant to the high-energy (001) planes with lowering of their surface free energy, identical to the phenomenon described above for aspartic acid adsorption on calcite steps. The adsorption of the surfactant inhibits the attachment of the solute molecules to this plane exposed at kink sites, slowing growth along the [001] direction so that growth along [010], relative to growth along [001], is increased.

Recent AFM studies of the growth biomolecular crystals, including proteins, viruses, and RNA crystals, in our laboratory and others,[39,40,42,64] have revealed that growth mechanisms similar to those described above for inorganic and organic crystals are operative, even though the fundamental units are macromolecular. For example, investigations in our laboratory have increased the understanding of the molecular organization processes responsible for insulin crystallization, the protein used for diabetes therapy. The self-association of insulin molecules and the organization of hexameric aggregates at an

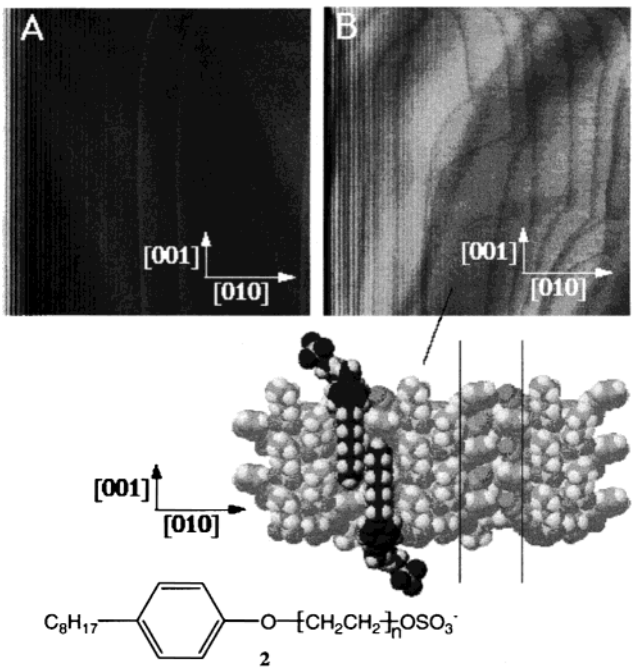

Figure 17. (top) AFM images (2 μm × 2 μm) of the (100) surface of a single crystal of the yellow dye **1**. The image on the left was acquired in water during active growth from a saturated solution of **1**. The image on the right was acquired during growth after adding the surfactant octylphenyl oligoether sulfate **2**. The image below is a schematic representation of the likely interaction of the surfactant with the crystal, in which the octyl tails nestle in troughs between surface butyl groups on the exposed (100) terrace, depicted by the vertical lines. This blocks access of solute molecules to the (001) face, which is required to kink propagation along the (010) steps, resulting in an increase in the relative growth rate on (010) and the appearance of the (001) steps that cause the curvature observed in the AFM images when surfactant is present.

actively growing crystal surface can be quite sensitive to small changes in the amino acid sequence. For example, Lys^{B28}Pro^{B29} insulin, in which the C-terminal prolyl and lysyl residues in the "B-chain" of the dual-chain wild-type human insulin are inverted, crystallizes as a rhombohedral form (*R*3 space group) that resembles wild-type insulins with respect to crystal structure and habit. The Lys^{B28}Pro^{B29} crystals exist as zinc-complexed hexamers organized into hexagonally ordered (001) layers as described for wild-type forms in Figure 12. However, tapping-mode atomic force microscopy (TMAFM) studies of single crystals of *R*3 Lys^{B28}Pro^{B29} reveal the influence of sequence variation on hexamer−hexamer association at the surface of actively growing crystals. Real-time TMAFM revealed hexamer vacancies on the (001) terraces of Lys^{B28}Pro^{B29} insulin crystals that were not observed on the wild-type crystals. Additionally, comparison of the screw dislocations on actively growing (001) faces of Lys^{B28}Pro^{B29} with wild-type porcine and bovine crystals reveals obvious differences in the curvature of the dislocation noses (i.e., the region of intersection of two steps) and in the terrace widths (identical to $T_{\pm}$ in the calcite description above but denoted here as λ_1 in order to be consistent with the original publication). Specifically, the terrace widths and nose curvature were signifi-

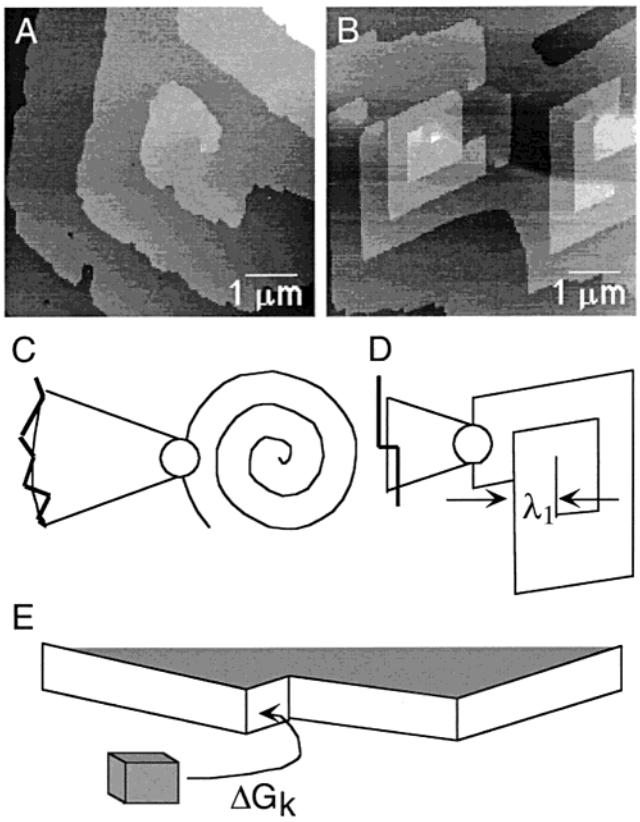

Figure 18. (A, B) Screw dislocations observed by in situ TMAFM under identical conditions for *R*3 $Lys^{B28}Pro^{B29}$ (A) and *R*3 porcine (B) insulin crystals. The step height is approximately 38 Å, equivalent to the c lattice parameter that defines a single (001) layer of insulin hexamers. (C,D) Schematic representations of rounded and sharp screw dislocations. The magnified regions illustrates that roughened ledges with numerous kink sites afford rounded dislocations, whereas smooth ledges with few kinks afford sharp dislocations. (E) Schematic representation of aggregate addition to a kink site on an exposed crystal terrace. The ledge interfacial energy and the free energy of kink addition are denoted by γ_l and ΔG_k, respectively. The rounded dislocations in (A) signify small ΔG_k values, which are synonymous with low surface energy for the kink planes that favors their formation. (Reprinted with permission from ref 64h.)

cantly larger for $Lys^{B28}Pro^{B29}$ than for porcine and bovine insulin (Figure 18).

These topographical features, which represent the nanoscale origins of the bulk crystal habit, stem from differences in surface energies and attachment free energies at the relevant crystal planes.[65] The radius of curvature of the dislocation nose (r_c) is equivalent to the critical nuclei radius of a stable two-dimensional nucleus. This radius is related to the surface energy of the ledges (γ_l) and the free energy of attachment at the kink sites that decorate the steps of the dislocation (ΔG_k) according to eq 5. This radius is also related to λ_l according to eq 6.

$$r_c = \frac{\gamma_l}{\Delta G_k} \tag{5}$$

$$\lambda_l = 4\pi r_c \frac{\gamma_l}{\Delta G_k} \tag{6}$$

A rounded dislocation nose is the consequence of roughened steps (i.e., many kinks) and slow growth parallel to the ledge direction. Large values of γ_l will favor rough steps and large terraces because the overall surface energy will be reduced by reducing the total area of the step planes which are parallel to the ledge direction. Small values of ΔG_k are synonymous with low surface energies for the kink sites, which will favor the formation of kink sites, roughening of the steps, and large λ_l values. Consequently, for a given γ_l, the net effect of a large ΔG_k is a screw dislocation with linear step edges and sharp corners. This is the behavior observed for the wild-type bovine and porcine insulin crystals. In contrast, a larger radius of curvature and the development of capes and protrusions at the edges of the screw dislocation were observed for $Lys^{B28}Pro^{B29}$, indicating a smaller ΔG_k and/or a larger γ_l compared to the wild-type insulins. Smaller ΔG_k values would be consistent with weaker interhexamer interactions, which is consistent with the appearance of point defects on the (001) terraces. These differences can be attributed to changes in protein conformation at the hexamer−hexamer interface and the resulting interhexamer association. These observations indicated subtle changes in molecular conformation due to a single sequence inversion in a region critical for self-association at the crystal interface. More important, the smaller ΔG_k values for $Lys^{B28}Pro^{B29}$ are consistent with more rapid dissolution of this insulin form, which may account for its increased pharmokinetic activity.

The influence of amino acid sequence on insulin organization during crystallization can be demonstrated further by the crystallization characteristics of the therapeutically important crystalline *ultralente* insulin forms, which are produced by crystallization in water with high salt concentrations. Characterization of these materials has been elusive because of small crystal size and poor diffraction characteristics. TMAFM studies of ultralente crystals prepared from bovine, human, and porcine insulins, performed directly in crystallization liquor, produced lattice images consistent with *R*3 space group symmetry for each insulin type. However, the *morphology* of the bovine insulin microcrystals, as observed by AFM, differs substantially from that of the human and porcine analogues. Whereas human and porcine ultralente crystals exhibited large molecularly flat (001) faces consisting of hexagonal arrays of close packed hexamers, bovine ultralente crystals predominantly exhibited faces with cylindrical features (Figure 19). These features are assignable to close-packed stacks of insulin hexamers laying in-plane, as expected for the (010) and (110) planes (Figure 20). This morphology was attributed to a 2-fold increase in the hydrophobic character of the upper and lower surfaces of the donut-shaped insulin hexamers in the bovine form compared to its human and porcine relatives, which results from minor sequence differences (Table 1). The increased hydrophobicity of these surfaces either promotes hexamer−hexamer stacking in precrystalline aggregates or enhances attachment of single hexamers at kinks decorating steps along

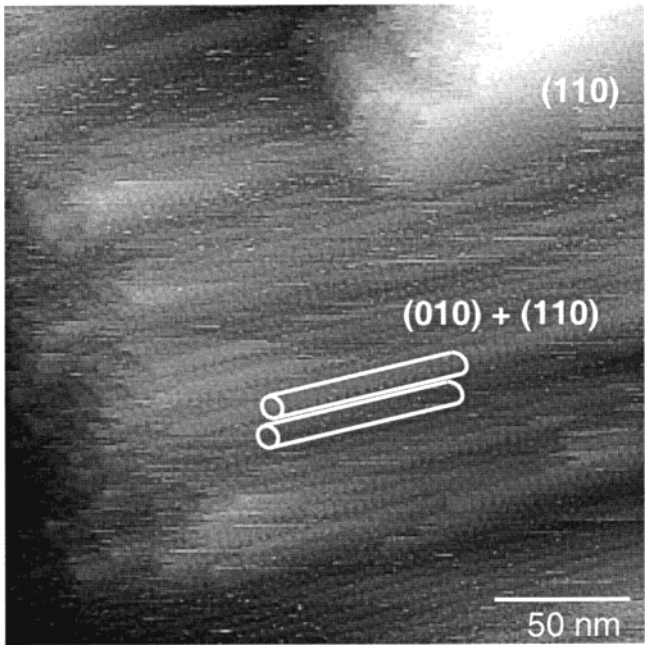

Figure 19. Tapping-mode AFM images of bovine insulin ultralente crystals acquired in crystallization liquor. Corrugated cylindrical features are evident on the large face. The cylinders are spaced at intervals of approximately 50 Å, and the interval between corrugations within a given cylinder is approximately 45 Å. Analysis of the images indicates that the crystal facets are assignable to the (010) and (110) planes of the *R*3 structure. (Reprinted with permission from ref 64j. Copyright 1998.)

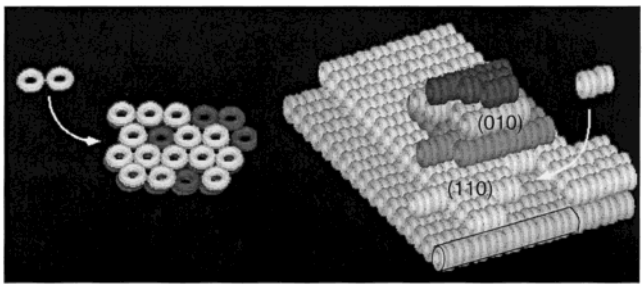

Figure 20. Schematic representation of the insulin hexamer packing on the prominent exposed crystal surfaces of (left) porcine (or human) insulin and (right) bovine ultralente insulin based on the *R*3 space group symmetry. At left the exposed surface is the (001) crystal plane, which is defined by close-packed hexagonal arrays of hexamers. This face, which predominates in porcine and human insulins, provides facile solvent access to the core of the insulin hexamer that contains the Zn^{2+} ion and to the solvent channels along the *c*-axis in the crystal. At right, the exposed surfaces correspond to the (010) and (110) crystal planes, which have close packed stacks of insulin hexamers that hinder solvent access to the crystal. The arrows depict possible mechanisms of ultralente crystal growth, which may occur by attachment of stacked hexamer aggregates to (010) or (110) planes in bovine insulin as shown at left or by attachment of single hexamers to growing (001) terraces in human/porcine insulins as depicted at right.

the [001] direction during crystal growth. Both events lead to enhanced growth of {*hk*0} planes instead of (001). The consequence of this mode of assembly is the predominance of close-packed (010) and (110) faces that prohibit solvent access to the center of the hexamers and to the interior of the crystal. This is consistent with the slower dissolution and longer basal activity of ultralente insulin formulations based on the bovine form. These observations demonstrated that subtle variations in amino acid sequence can dramatically affect the interfacial structure of crystalline proteins, with implications for the design of therapeutic protein formulations, Table 1.

Table 1. Amino Acid Sequences for Bovine, Human, and Porcine Insulins for Residues 6−12 of the Insulin A Chain[a]

A-chain residue number	6	7	8	9	10	11	12
bovine	Cys	Cys	**Ala**	Ser	**Val**	Cys	Ser
human	Cys	Cys	**Thr**	Ser	**Ile**	Cys	Ser
porcine	Cys	Cys	**Thr**	Ser	**Ile**	Cys	Ser

[a] Those residues that differ are bold.

An AFM investigation of the growth of urea inclusion compounds (IUCs) is particulary insightful with respect to molecular organization at the crystal growth interface.[66,67] IUCs are crystalline phases in which urea forms a hexagonal lattice of one-dimensional channels that contain linear guest molecules such as alkanones and alkanediones. These phases may be either commensurate, poorly commensurate, or incommensurate with respect to the guest and host repeat distances (c_g' and c_h', respectively) along the channel direction. Interestingly, the degree of commensurism influences crystal growth on the (001) faces, which is the plane perpendicular to the channel direction (Figure 21).

Highly commensurate phases exhibit large terrace areas, with the terraces separated by steps equal to the length of the guest molecule (Figure 22). In contrast, poorly commensurate phases exhibited highly roughened surfaces. This behavior can be interpreted in terms of a molecular roughness factor related to the degree to which a guest molecule protrudes from a terrace surface. If incommensurate guest molecules protrude from channels exposed at a terrace, they will provide high-energy sites for 2-D nucleation of urea, leading to a roughened surface. However, if the IUC is commensurate, the host can wrap around the guest molecule such that the terminus of the guest no longer protrudes from the host. Successive attachment to facets of the resulting host−guest column leads to rapid growth in the lateral direction. The guest species are relatively mobile in the urea channels, and it is likely that nucleation of these terraces is instigated by guest molecules that momentarily protrude from the surface.

These examples are illustrative of the molecular organization processes that occur during homoepitaxial growth of single crystals. Most important, these examples demonstrate that the principles that govern crystallization are universal and transcend the type of material and the length scale that defines the structural order—from inorganic to organic to protein crystals. In most cases the surface topography and growth modes during crystallization can be correlated with the structure and bonding anisotropy in the crystal. AFM allows direct visualization of molecular assembly processes at actively growing crystal interfaces, which are dramatically affected by crystal structure and anisotropy, adsorption of for-

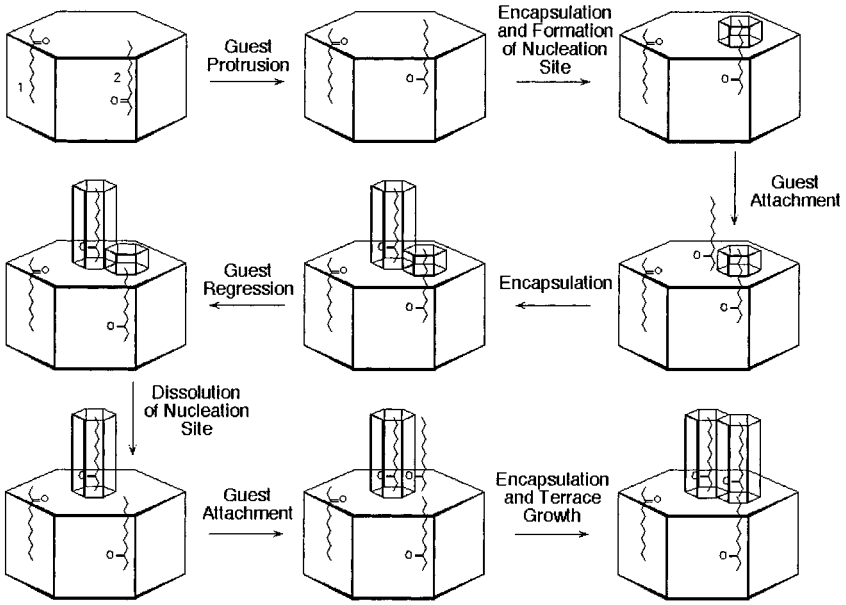

Figure 21. Template-directed mechanism for nucleation and crystal growth on a crystal terrace along the channel axis of urea inclusion compounds. In the case of a commensurate UIC, the length of the an alkanone guest is equal to an integral multiple of the urea host repeat distance and the guest will not protrude from the surface. If guest 2 momentarily protrudes to generate a site for urea growth, the tip of the guest is encapsulated by host, producing an attachment site for an incoming guest molecule. Encapsulation of this attached guest molecule results in a column on the terrace that can serve as the site of further attachment of guest molecules and their encapsulation to form a terrace whose thickness corresponds to the length of a single guest molecule. Successive addition of guest and host to the nanoscopic facets of this growth feature favor lateral growth to build the terrace in two dimensions. If the UIC is commensurate, guest 2 most likely regresses to its original position, resulting in dissolution of the vacated feature. (Reprinted with permission from ref 67. Copyright 1997.)

eign molecules, or, in the case of proteins, by very minor changes in protein sequence.

B. Heteroepitaxial Nucleation

1. Principles of Nucleation

Prior to growth of a macroscopic, stable crystal, solute molecules must aggregate to form a nucleus that at some stage must have a structure that resembles the bulk crystal structure. This nucleation process requires organization which is entropically unfavorable owing to the increase in order accompanying the assembly process. Initially nucleation is also *enthalpically* unfavorable because of the phase boundary between the nucleus and the solution that has a specific surface energy associated with unsatisfied bonding of the solute molecules at this interface. The entire process is generally described by a simple homogeneous nucleation model,[68] in which the total free energy of nucleation for a spherical particle can be described as the sum of two terms according to eq 7

$$G_{tot} = -^4/_3\pi r^3 G_v + 4\pi r^2\gamma \qquad (7)$$

where r is the radius of the nucleus, G_v is the free energy per unit volume, and γ is surface energy associated with the surface area of the nucleus. The first term represents the favorable volume free energy associated with nucleus formation, whereas the second term represents the energy penalty associated with creation of the phase boundary. These opposing contributions result in a G_{tot} that exhibits a maximum at r^*, the critical radius (Figure 23). Solving for $dG_{tot/dr} = 0$ for r affords the numerical value of r^* and the corresponding activation energy for the nucleation process, G^*, as given by eqs 8 and 9. When $r < r^*$, the surface energy dominates and the aggregate is unstable toward dissolution, but when $r > r^*$, the volume free energy term dominates.

$$r^* = \frac{-2\gamma}{G_v} \qquad (8)$$

$$G^* = \frac{16\pi\gamma^3}{3G_v^2} \qquad (9)$$

Although the homogeneous nucleation model is insightful, *true homogeneous nucleation is a rare occurrence* because of the energetic penalty associated the creation of the phase boundary between the growing nucleus and the growth medium. Consequently, nucleation of a new crystalline phase almost always occurs on the surface of a foreign substance, although this is not always recognized because the foreign substance may not be readily detectable. Nucleation of a crystalline phase on a surface can be described by a disk-shaped aggregated with radius r and a height corresponding to one atomic or molecular layer. If the surface energy contribution of the growth substrate is ignored (this would only make heterogeneous nucleation even more favorable), the

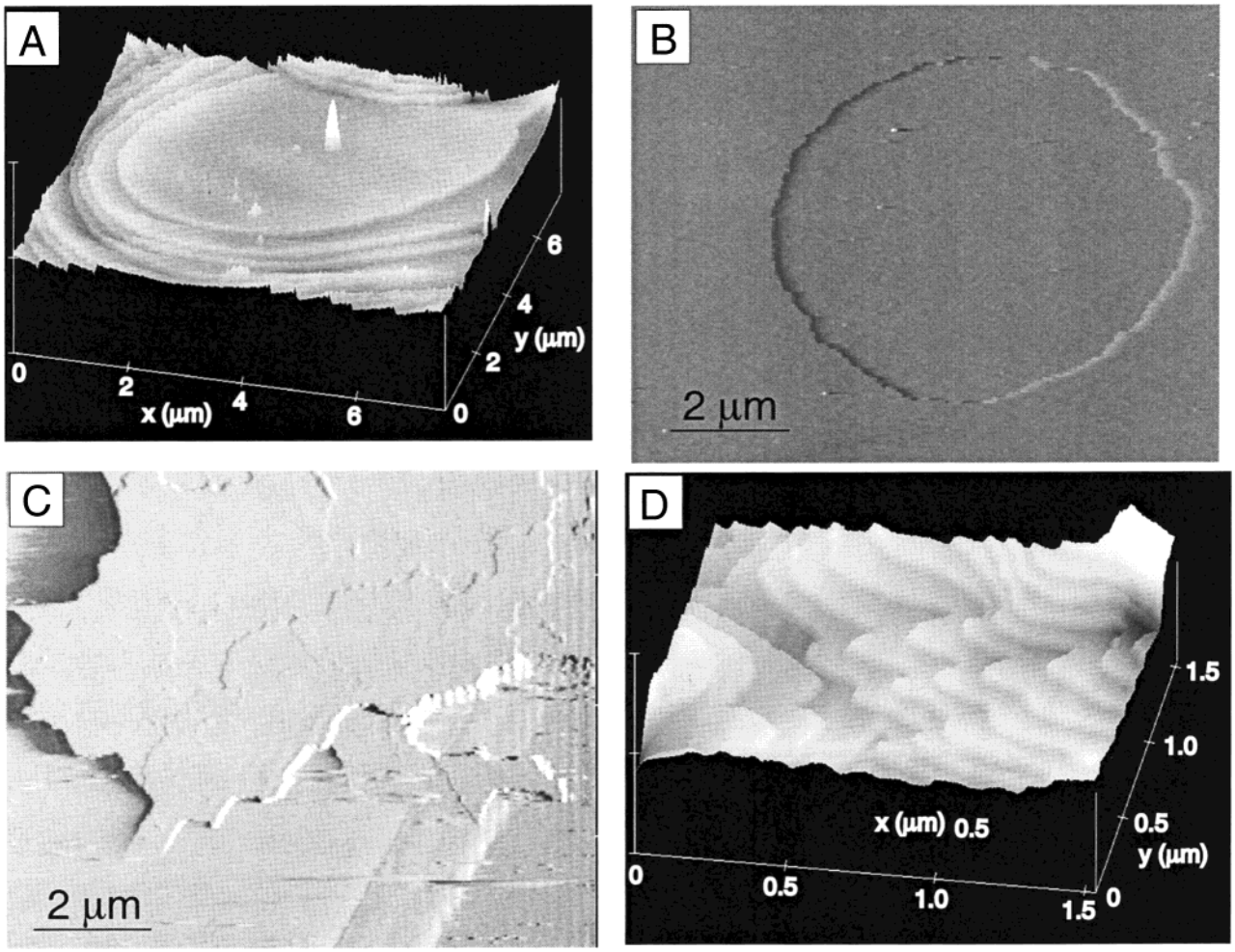

Figure 22. Mechanism depicted in Figure 21 is supported by AFM data which demonstrates (A) large flat terraces for commensurate 2,9-decanedione/urea ($3c'_g = 4c'_h$) with step heights of 15.7 Å, (B) flat terraces during dissolution of the highly commensurate 2,10-undecanedione/urea ($2c'_g = 3c'_h$), as imaged in a slightly undersaturated solution of 9:1 urea: guest in *t*-amyl alcohol, but (C) rather rough terraces for 2,11-dodecanedione/urea, which has poorer commensurism ($12c'_g = 19c'_h$). (D) Crystals of the commensurate 8-pentadecanone/urea exhibit molecularly flat terraces, consistent with the mechanism in Figure 21. In A, B, and D the step heights correspond to the length of the molecular guests. (Reprinted with permission from ref 67. Copyright 1997.)

total free energy, activation energy, and critical radius can be described by eqs 10−12. Both G^* and r^* are less than the homogeneous counterpart.

$$G_{tot} = -\pi r^2 G_v + 2\pi r\gamma \qquad (10)$$

$$G^* = \frac{\pi\gamma^3}{G_v^2} \qquad (11)$$

$$r^* = \frac{-\gamma}{G_v} \qquad (12)$$

Although the importance is well recognized, the understanding of heterogeneous nucleation with respect to the molecular organization can best be described as embryonic. Nucleation can occur on the surface of a foreign substance, amorphous or crystalline, such as the sides of a glass beaker or a purposely introduced seed. The total free energy description, modified to include interfacial energy terms associated with the substrate−liquid, nucleus−liquid, and substrate−nucleus interfaces, can be described by eq 13

$$G_{tot} = VG_v + \gamma_{nl}A_{nl} + (\gamma_{sn} - \gamma_{sl})A_{sn} \qquad (13)$$

where V is the volume of the nucleus, A_{nl} is the surface area of the solution−nucleus interface, A_{sn} is the surface area of the nucleus−substrate interface, and ΔG_v is the free energy change per unit volume. The terms γ_{nl}, γ_{sn}, and γ_{sl} are the interaction energies per unit area of the solution−nucleus, nucleus−substrate, and solution−substrate interfaces, respectively (Figure 23).[69] This relationship indicates that (1) if γ_{sn} is less than γ_{sl} the average surface energy of the system decreases and the substrate acts to enhance nucleation,[70] (2) nucleation becomes more favorable with increasingly negative γ_{sn} values, (3) if γ_{sn} is negative nucleation becomes more favorable as the area of contact between the nucleus and substrate increases, (4) nucleation is favored not only because of the formation of a favorable substrate−nucleus interface but also be-

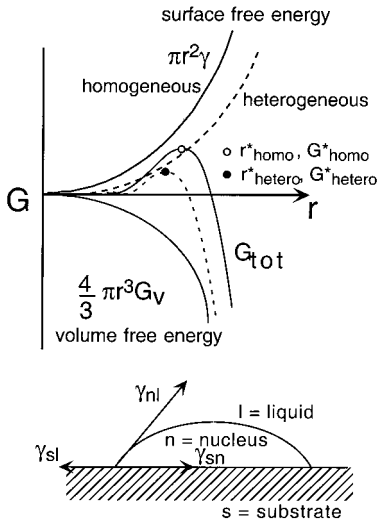

Figure 23. (top) Dependence of the total free energy on the radius of a spherical nucleus for homogeneous and heterogeneous nucleation. The critical radius, r^*, and the activation energy for nucleation, G^*, are both reduced when nucleation occurs on a substrate. (bottom) Schematic representation of a hemispherical nucleus on a substrate surface. The angle θ is the wetting angle, and γ_{nl}, γ_{sn}, and γ_{sl} are the interaction energies per unit area of the solution−nucleus, nucleus−substrate, and solution−substrate interfaces, respectively.

cause of the reduction in area of the substrate−liquid interface.

The relationship between the surface energies and the contact angle formed by the nucleus and the substrate, θ, is given by eq 14

$$\gamma_{sl} = \gamma_{sn} + \gamma_{nl}\cos\theta \tag{14}$$

Consequently, the activation energy for nucleation can be described by an expression that includes a function $f(\theta)$ according to eqs 15 and 16. Decreasing values of θ for $\theta < 90°$ (so that $f(\theta) < 1$) lowers the energy barrier for nucleation. This is equivalent to stating that nucleation is preferred for systems in which the nucleus strongly "wets" the substrate.

$$\Delta G^*_{hetero} = \Delta G^*_{homo}\, f(\theta) \tag{15}$$

$$f(\theta) = {}^1/_4(2 + \cos\theta)(1 - \cos\theta)^2 \tag{16}$$

Conventional models that have been advanced for thin film growth are instructive for understanding the degree of "wetting" of a substrate by an incipient nucleus (Figure 24). The Frank−van der Merwe mode describes the condition of strong attraction between the molecules of a film and a substrate, leading to layer-by-layer growth, typically observed if an epitaxial relationship exists between the film and substrate. Volmer−Weber growth is observed when the attraction between molecules of the film is stronger than that between the film and the substrate so that the film tends to coalesce as three-dimensional islands rather than wetting the substrate. The intermediate case, Stranski−Krastanov growth, is described by the initial formation of a film layer followed by island growth on that layer. This can result if there is a slight lattice mismatch, but

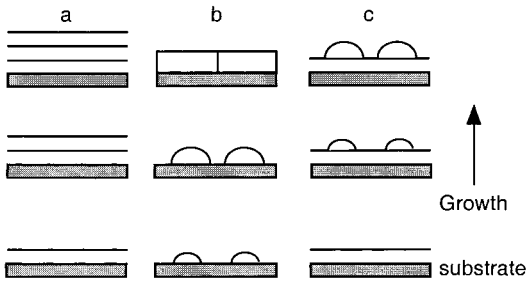

Figure 24. Schematic of film growth modes: (a) Frank−van der Merwe, (b) Volmer−Weber, and (c) Stranski−Krastanov.

still favorable interaction, between the film and substrate. This creates a strain in the initial layer that makes layer−layer interactions less favorable, thereby promoting the formation of three-dimensional islands of the material, with its native structure, on the primary layer.

The consequences of heterogeneous nucleation on a surface are apparent—the critical radius and the activation energy are both reduced. Therefore, heterogeneous nucleation will almost always be preferred over its homogeneous counterpart. In a typical crystallization vessel, the substrate interface for heterogeneous nucleation may not always be known, but elucidation of the principles for growth at the substrate−nucleus interface can lead to intelligent design of nucleation substrates so that nucleation kinetics can be rationally directed. The ability to tune the kinetics of crystallization of specific crystal forms can be crucial to controlling polymorphism, a key issue in the processing of numerous organic crystals.

2. Epitaxy and Nucleation on Two-Dimensional Substrates

The wetting models described in the previous section, while instructive from the standpoint of general principles, do not provide an engineering strategy for controlling heterogeneous nucleation. A reasonably straightforward approach to controlling heterogeneous nucleation is one that relies on the interaction between incipient nuclei and a nucleation substrate surface that serves as a precise structural and stereochemical mimic of a specific crystal plane, whose structure is deduced from the known 3-D crystal structure of the crystallizing phase. This approach has been used to direct the nucleation of organic crystals beneath highly ordered Langmuir monolayers formed at an air−water interface. The monolayer thereby lowers the activation energy for nucleation through precisely matched interactions between the monolayer headgroups and the matching lattice plane of the nucleus (negative γ_{sn} in Figure 23) while reducing the surface energy of the nucleus by eliminating one of the surfaces in contact with the growth medium (reduced A_{nl}). Several reviews have appeared on this subject, primarily based on elegant work performed at the Weizmann Institute.[71,72] Recent GIXD studies are beginning to unravel the structural relationships between Langmuir monolayers that behave as structural mimics and incipient nuclei.[73]

The organization of molecules of incipient nuclei at the Langmuir monolayer interface can be de-

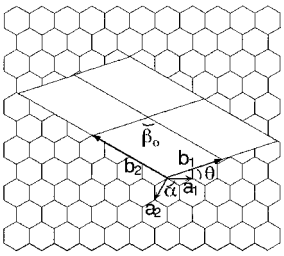

Figure 25. Schematic representation of four unit cells of a generic crystalline layer B on an ordered substrate A. The substrate and layer lattices are defined by two-dimensional cells with lattice constants a_1, a_2, α and b_1, b_2, β, respectively. The angle θ represents the angle between the vectors $\mathbf{a_1}$ and $\mathbf{b_1}$ defining the azimuthal angle of the overlayer with respect to the substrate.

scribed as commensurate, in which the position of each molecule of the contacting plane of the nucleus sits on a site of the ordered Langmuir substrate "surface." Indeed, the concept of commensurism is a familiar one generally used to describe the arrangement of stable adlayers of molecules on a surface of a *solid* crystalline substrate. However, given the low space group symmetry of most organic crystals, it is likely that the incipient nucleus can only contact the substrate with a crystal plane having an oblique, low-symmetry geometry. The two-dimensional interface consisting of substrate A and layer B can be generally described by seven parameters (Figure 25). The substrate layer A, depicted here as having hexagonal symmetry, has lattice constants a_1, a_2 and angle α and layer B by b_1, b_2 and angle β, and the azimuthal orientation can be defined by the angle θ between vectors $\mathbf{a_1}$ and $\mathbf{b_1}$. In the case of homoepitaxial crystal growth, $a_1 = b_1$, $a_2 = b_2$, $\alpha = \beta$, and $\theta = 0°$. An oblique unit cell cannot be commensurate with the hexagonal substrate; in fact, the layers must have identical symmetry for the interface to be commensurate. However, low-symmetry organic layers and their nuclei can be stabilized by *coincident* epitaxy, which was first observed for simple atomic systems such as the (111) planes of fcc Ni, Cu, Au, and Ag on the (110) plane of bcc tungsten[74] but has largely been ignored for heterogeneous nucleation of organic films and crystals.

The azimuthal relationship between substrate A and overlayer B can be defined by a transformation matrix **C** that relates $\mathbf{b_1}$ and $\mathbf{b_2}$ to $\mathbf{a_1}$ and $\mathbf{a_2}$, where **C** is a 2 × 2 matrix with elements p_x, q_y, q_x, and p_y (eq 17). The values of the matrix elements depend on the substrate lattice constants, the overlayer lattice constants, and θ according to eqs 18−21.

$$\begin{bmatrix} b_1 \\ b_2 \end{bmatrix} = [\mathbf{C}] \begin{bmatrix} a_1 \\ a_2 \end{bmatrix} = \begin{bmatrix} p_x & q_y \\ q_x & p_y \end{bmatrix} \begin{bmatrix} a_1 \\ a_2 \end{bmatrix} \tag{17}$$

$$p_x = b_1 \sin(\alpha - \theta)/a_1 \sin(\alpha) \tag{18}$$

$$q_y = b_1 \sin(\theta)/a_1 \sin(\alpha) \tag{19}$$

$$q_x = b_2 \sin(\alpha - \theta - \beta)/a_1 \sin(\alpha) \tag{20}$$

$$p_y = b_2 \sin(\alpha + \theta)/a_2 \sin(\alpha) \tag{21}$$

Commensurism exists when each overlayer lattice point resides on a substrate lattice point. Under this condition, det(**C**) and each of the matrix elements assume integral values. Det(**C**) for incommensurism, when the overlayer exhibits no periodic lattice matching with the substrate, has irrational values. *Coincidence* exists when a fraction of the overlayer lattice points coincide with substrate sites at periodic intervals. The det(**C**) of the aforementioned matrix (eq 17) is a simple fraction for a coincident lattice. This may be important for crystalline organic films, which tend to have low symmetry and therefore cannot be commensurate with high-symmetry substrates. Given the diverse variety of organic films that have been reported, for example, anthrone derivatives,[75,76] oligothiophenes,[77] tetrathiafulvalene-based salts,[11,27,78] mesogenic molecules with liquid crystal properties,[79,80,81] perylenetetracarboxylic acid dianhydride and diimide,[82,83,84,85] phthalocyanine,[86,87,88] and hexabromobenzene,[89] such symmetry considerations are important.

A distinguishing feature of coincident epitaxy is the existence of a nonprimitive overlayer supercell that contains an integral number of overlayer unit cells. The supercell can be constructed such that its corners coincide periodically with substrate lattice points, but overlayer lattice points within the boundaries of the supercell do coincide with substrate lattice points. It has been shown that many molecular overlayers actually exhibit point-on-line (POL) coincidence with inorganic substrates such as HOPG and MoS_2. This special, but common, type of coincidence has *rows* of overlayer sites that coincide periodically with uniformly spaced rows of substrate sites corresponding to a specific substrate lattice direction. Under this condition, one of the reciprocal lattice vectors of the overlayer has the same direction as the reciprocal lattice vector defined by the substrate rows (Figure 26). The magnitude of the overlayer reciprocal lattice vector is an integer multiple of the corresponding substrate lattice vector; therefore, these reciprocal lattice vectors ($\mathbf{a_2}^*$ and $\mathbf{b_2}^*$) can be considered commensurate. POL coincidence further requires that certain combinations of the matrix coefficients assume integral values at the rotation angle θ. In the case of a generic lattice, p_x and q_x or p_y and q_y must be integers. Integral values for these combinations, or for the sums $p_x + q_y$ and $q_x + p_y$, will produce coincidence on hexagonal substrates.

Although the degree of epitaxy is less for coincident overlayers than for truly commensurate ones, the overlayer lattice points at the corners of the supercell that coincide periodically with substrate lattice points provide the energy lowering required to stabilize the overlayer in a preferred azimuthal orientation. If these positions are energetically most favorable, by inference the other noncoinciding overlayer positions must be less energetically favorable. This could be avoided if the layer expanded to the extent that all the molecules sit on substrate lattice points so that commensurism is attained. However, this carries an energetic penalty with respect to the loss of intermolecular bonding within the layer. The structure of an overlayer therefore reflects the balance between the overlayer−substrate interactions and intralayer interactions. However, if the substrate is to stabilize

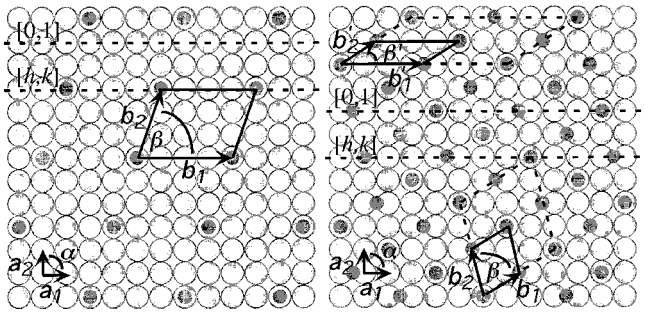

Figure 26. Schematic representation of commensurism and coincident epitaxy. Overlayer lattice points are depicted as small filled circles, substrate lattice points are depicted as larger shaded circles, and the overlayer primitive cells are indicated by solid lines. (a) In a commensurate overlayer, every overlayer lattice point coincides with a substrate lattice point and certain overlayer [*h*,*k*] lines, in this case [1,4] overlayer lattice lines, coincide with primitive [0,1] substrate lines. (b) POL-coincident overlayers require that all four matrix elements be rational with two integers confined to one column. All overlayer lattice points, here distributed on overlayer [1,2] lattice lines, must lie on a particular primitive substrate line, here [0,1]. The 2 × 2 supercell for this overlayer is indicated by dashed lines connecting the supercell corners. An alternative choice of the primitive unit cell is depicted by lattice vectors $\bar{b}_1'$ and $\bar{b}_2'$. The area and transformation matrix determinants are identical for both cells.

an overlayer that is an incipent nucleus of a given crystalline material, it is preferable that the overlayer retain a "native" structure corresponding to a specific crystal plane in the mature crystal.

The displacement of the noncoinciding positions from energetically ideal positions can be considered as a strain within the overlayer−substrate interface. Similarly, changes in the overlayer structure required to achieve commensurism (or even coincidence) can be considered as an intralayer strain with respect to a native structure. Therefore, the likelihood of commensurate or coincident lattices is determined by stresses at the overlayer−substrate interface resulting from these strained positions. Numerous examples of organic films have demonstrated that if the substrate−layer interface is dominated by van der Waals interactions, the potential wells are relatively shallow and the energetic penalty of the noncommensurate positions does not dominate for reasonable supercell sizes. Shallow potential functions are synonymous with small elastic constants, which can be calculated from the second derivative, d^2V/dx^2, of the potential function, where x represents displacement of the molecule along a substrate direction (the second derivative a measure of the curvature at the energy minimum). A small elastic constant for the layer−substrate interface represents a small energetic penalty associated with displacement from the energy minimum along a specified direction. If the interface stresses are smaller than the intralayer stresses that would accompany formation of a less close-packed, but commensurate, structure, the overlayer will tend to retain a preferred native structure and, if possible, adopt a coincident epitaxial configuration. This condition tends to favor coincidence involving low-index, close-packed molecular planes that generally have the largest intralayer elastic constants.

Models of the epitaxial interface have been devised that provide insight into the structure and formation of these films and their orientational relationship to the substrate.[90−93] Coincident configurations are difficult to visualize without the aid of computer modeling. A recent algorithm developed in our laboratory, implemented in a program named EpiCalc, enables rapid determination of the mode of epitaxy and preferred azimuthal angle, θ, for a given overlayer and substrate.[77] This routine relies on the calculation of a "dimensionless potential", V/V_o, that derives from lattice misfit calculations based on a function that relates the lattice parameters of the overlayer to those of the substrate according to eq 22. V/V_o assumes discrete values of 0, 0.5, and 1.0 for commensurate, coincident, and incommensurate films. This approach simply relies on the superposition of plane waves corresponding to the symmetry and dimensions of the two opposing lattices, which in turn correspond to the surface potentials of the two lattices.[94] The method is similar to one described by Reiss for rigid square lattices [95] and later by van der Merwe for rectangular lattices of identical symmetry.[96] EpiCalc also enables calculation of the supercell size for coincident layers. Lattice misfit modeling with this routine has demonstrated that many reported organic overlayers on a variety of substrates are organized through coincident epitaxy, including ones that had been regarded as incommensurate.

$$V = {}^1/_2V_o\left[2 - \cos\left(\frac{2\pi x}{a_x}\right) - \cos\left(\frac{2\pi y}{a_y}\right)\right] \qquad (22)$$

The role of coincident epitaxy and the process of molecular organization during crystallization of ordered 2-D films can be illustrated by overlayers of bis(ethylenedithiolo)tetrathiafulvalene (ET) and triodide ions on highly oriented pyrolytic graphite (HOPG), generated by electrochemical oxidation of ET in the presence of I_3^-.[97] In situ AFM during growth revealed the gradual formation of continuous islands with a thickness of 15 Å (Figure 27). This height, and lattice images acquired on the surface of the film during growth, indicated that the structure of the film was highly crystalline and identical to the structure of (001) molecular layers present in β-$(ET)_2I_3$. This phase is one of numerous polymorphs and compositional variants containing these components. The molecular orientation in the film preserves the strong $\pi-\pi$ charge-transfer interactions between ET molecules along the stacking direction and strong intermolecular S···S interactions between stacks. The azimuthal orientation of the overlayers with respect to the HOPG lattice can be determined by imaging the overlayer and substrate in the same image frame.

The AFM data indicated that the β-$(ET)_2I_3$ a lattice vector was rotated 19° (θ = 19°) with respect to the a_1 graphite lattice vector, identical to the value predicted from the excursion to $V/V_0 = 0.5$ in lattice modeling calculations with EpiCalc. This coincident configuration produces a $1\mathbf{b_1} \times 3\mathbf{b_2}$ supercell with corners that coincide with HOPG substrate sites at

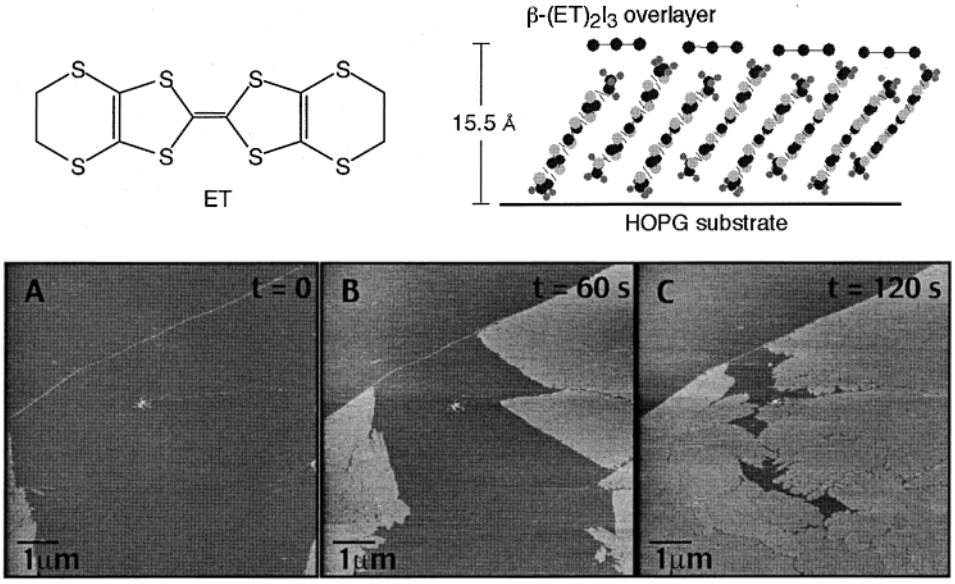

Figure 27. In situ AFM images acquired during electrochemical growth of the Type I β-$(ET)_2I_3$ (001) overlayer on a freshly cleaved HOPG electrode at t = (a) 0, (b) 60, and (c) 120 s, following a potential step to E_{cryst} = 650 mV (vs Ag/AgCl). The overlayer thickness is 15.5 Å. The linear feature on the HOPG surface in the middle of each image corresponds to one of the $\{\bar{1}2\bar{1}0\}$ principal lattice vectors of HOPG ($\mathbf{a_1}$ or $\mathbf{a_2}$).

periodic intervals (Figure 28). The other predominant polymorph, β-$(ET)_2I_3$, does not form on HOPG due to the absence of an epitaxial match with the (001) layer.

The 3-fold symmetry of the HOPG substrate resulted in azimuthally rotated crystalline domains of the β-$(ET)_2I_3$ overlayer related by $\pm n60°$. The domains in β-$(ET)_2I_3$ overlayers are distinguished readily by lateral force microscopy, which revealed different force contrast among the domains due to the molecular anisotropy of the monolayer surface, which causes the tip to experience differently oriented molecular fields on rotated domains (Figure 29). Furthermore, the domain boundaries are revealed by enhanced friction due to disorder in these regions that decreases the rigidity of the film in these regions. Previous studies have suggested that friction is greater for domains with lesser order and lower moduli due to greater penetration of the tip in softer phases. Electrochemical "annealing", in which the electrochemical potential was cycled repeatedly about the deposition and dissolution potential, eliminated these domains, similar to nonelectrochemical annealing of 2-D crystals of 2-hexadecyl-anthraquinone and tetradodecyl-octathiophene.[98,] Real-time AFM of the β-$(ET)_2I_3$ domains during annealing revealed that the film dissolved preferentially at the domain boundaries where the line energy is large,[99] with dissolution occurring more rapidly at the boundaries of domains having larger perimeter-to-area ratios.[27]

In contrast to the (001) β-$(ET)_2I_3$ overlayers, $(ET)_2$-ReO_4 overlayers exhibit a dramatically different orientation that resembles the (011) layers of bulk $(ET)_2ReO_4$. Even though the (001) layer is coincident, its formation requires a rather large supercell ($3\mathbf{b_1} \times 4\mathbf{b_2}$) associated with this orientation. This leads to a substantial accumulation of interfacial stresses from the large number of noncoinciding overlayer positions within the supercell. Rather, the AFM data revealed the formation of the (011)-type layers in which intermolecular S···S are lost but coincidence is attained with a substantially smaller supercell, thereby minimizing the number of noncoinciding positions in the overlayer. These observations demonstrate that the organization of molecules into 2-D crystals on substrates is governed by a delicate balance of intralayer and overlayer-substrate energetics but that epitaxy is crucial to the stabilization of these crystalline arrays of molecules. The use of epitaxial concepts provides a "crystal engineering" approach to the fabrication of molecular thin films.

Coincident epitaxy may not necessarily be limited to organization on solid substrates. Langmuir monolayers based on quasihexagonal hydrogen-bonded networks of 1-octadecanesulfonate amphiphiles and guanidinium ions, with a structure identical to the hydrogen-bonding networks in related crystalline phases (Figure 2), promote the nucleation of (100) oriented diphenyl sulfone (DPS) crystals. This is somewhat surprising because the conventionally accepted mechanism for nucleation under Langmuir monolayers—mimicry of a specific crystal plane and molecular recognition of the nucleant by the monolayer—is absent here. Furthermore, the hexagonal symmetry of the monolayer and rectangular (100) plane does not allow commensurism. Therefore, it is likely that nucleation involves *coincident epitaxy* between the monolayer and the (100) face. Analysis of the monolayer−DPS (100) interface with lattice misfit modeling reveals a POL coincident epitaxial match at $\theta = 4.66°$, where θ is the angle between the [010] vector of DPS and the $\mathbf{a_1}$ vector of the monlayer, defined as the direction between nearest neighbor sulfonates. This observation indicates that the design principles for nucleation beneath Langmuir monolayers can be broadened significantly.

3. Ordered Molecular Adlayers on Solid Substrates

While the examples above illustrate that numerous organic crystal surfaces and two-dimensional crystals

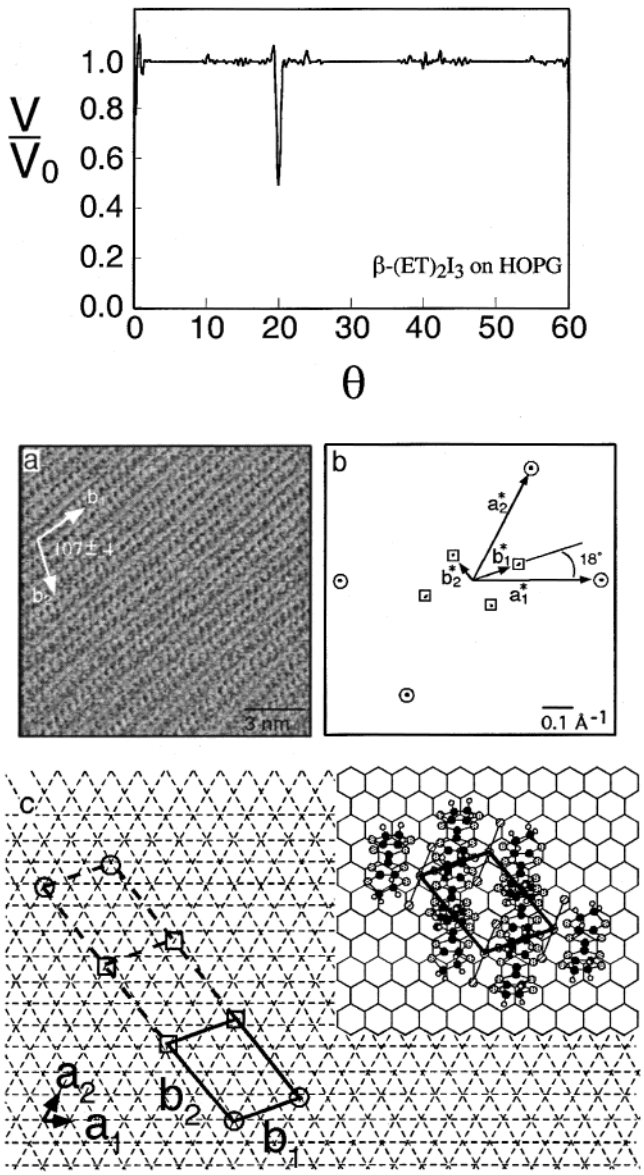

Figure 28. (top) EpiCalc output for a β-$(ET)_2I_3$ (001) overlayer on HOPG (a) AFM lattice image of the Type I overlayer acquired in situ under growth conditions. The lattice parameters determined from the real space, and Fourier data are $b_1 = 6.2 \pm 0.5$ Å, $b_2 = 9.4 \pm 0.8$ Å, and $\beta = 107 \pm 4°$. (b) Fourier spectra of the β-$(ET)_2I_3$ (001) overlayer and the HOPG substrate illustrating the relationship between the reciprocal lattice vectors $\mathbf{a}_1$*, $\mathbf{a}_2$* of HOPG (○) and $\mathbf{b}_1$*, $\mathbf{b}_2$* of the β-$(ET)_2I_3$ overlayer (□). These data reveal that the lattice vectors $\mathbf{a_1}$ and $\mathbf{b_1}$ subtend an angle of $\theta = 18°$. (c) Schematic representation of the $1\mathbf{b_1} \times 3\mathbf{b_2}$ supercell of a (001) β-$(ET)_2I_3$ overlayer lattice on HOPG. The open squares represent the overlayer lattice points that exhibit point-on-line concidence, whereas the open circles define the supercell corners the coincide with substrate lattice points. The right side of the figure illustrates the molecular motif of the Type I β-$(ET)_2I_3$ (001) overlayer on a conventional representation of the HOPG surface.

can be readily characterized with AFM, the direct observation of molecular adlayers that are specifically bound to surfaces are limited. These adlayers, particularly ones that are loosely packed, can be sensitive to the forces exerted by the tip during imaging. As discussed in section II.B.2, these forces can be reduced considerably if imaging is performed in suitable fluids. This was demonstrated in our laboratory for the formation of organized adlayers of molecular anions on the (0001) surface of hydrotalcite (HT), a layered clay with the composition $Mg_6Al_2(OH)_{16}CO_3{\cdot}4H_2O$. This adsorption process was believed to mimic the ion exchange reactions that commonly occur within the layers of hydrotalcite and other layered clays, which have significant technological interest due to their utility as ion-exchange materials,[100] catalysts,[101] antacids,[102] and catalytic supports.[103]

HT exists as hexagonal plates in the rhombohedral *R*-3*m* space group and consists of cationic brucite-like $Mg_6Al_2(OH)_{16}^{2+}$ layers with hexagonal symmetry, separated by layers of charge-compensating hydrated carbonate anions. AFM images of (0001) surfaces of HT acquired in aqueous solutions revealed an ordered hexagonal structure with a lattice constant of 6.4 ± 0.3 Å, in agreement with $a = 6.2$ Å expected for this surface. The HT sheet exposed at the outer crystal surface has two important characteristics: (i) one unit of excess positive charge for every eight metal atoms because of incomplete charge compensation by the interstitial CO_3^{2-} ions (these surfaces can therefore be regarded as $Mg_6Al_2(OH)_{16}^{1+}$), which must be compensated by anionic species from solution and (ii) exposed triads of hydroxyl groups that can serve as hydrogen-bonding adsorption sites. These features govern the adsorption of the anions (1− or 2−) of the organic diacid 5-benzoyl-4-hydroxy-2-methoxybenzenesulfonic acid (MBSA),[104] which is known to intercalate into HT.[105] Molecular models suggested that the 3-fold symmetry and size of the sulfonate group on the MBSA anion are ideally suited for hydrogen-bonding interactions with the hydroxyl group triads (Figure 31), while the negative charge of the anions compensates for the excess positive charge of the exposed HT surface.

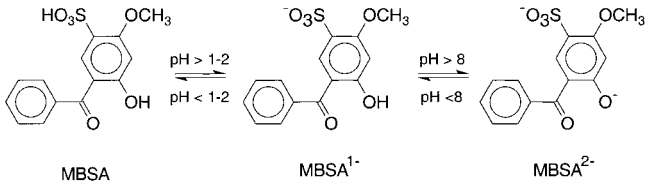

In aqueous media at pH = 10.5, at which $MBSA^{2-}$ is the predominant species in solution, AFM revealed the formation of a highly ordered adlayer with lattice constants of $a = 9.6 \pm 0.4$ Å and $b = 18.2 \pm 0.4$ Å (Figure 32). If each major feature in the data is assigned to a $MBSA^{2-}$ anion, the surface coverage is $\Gamma = 1.06 \times 10^{-10}$ mol cm^{-2}. A structural model that (i) accounts for this coverage, (ii) places the sulfonate group of each anion on hydroxyl triads, and (iii) maintains electroneutrality can be constructed with lattice constants of $a = 9.3$ Å and $b = 18.6$ Å, similar to the values deduced from the contrast in the AFM image.

Reducing the solution pH to 6.6, at which the solution is rich in $MBSA^{1-}$, produces a zigzag row structure with two major features contained in an area bounded by a lattice with constants of $a = 8.0 \pm 0.2$ Å and $b = 19.3 \pm 0.2$ Å. The data are consistent with a surface coverage of $\Gamma = 2.41 \times 10^{-10}$ mol cm^{-2}.

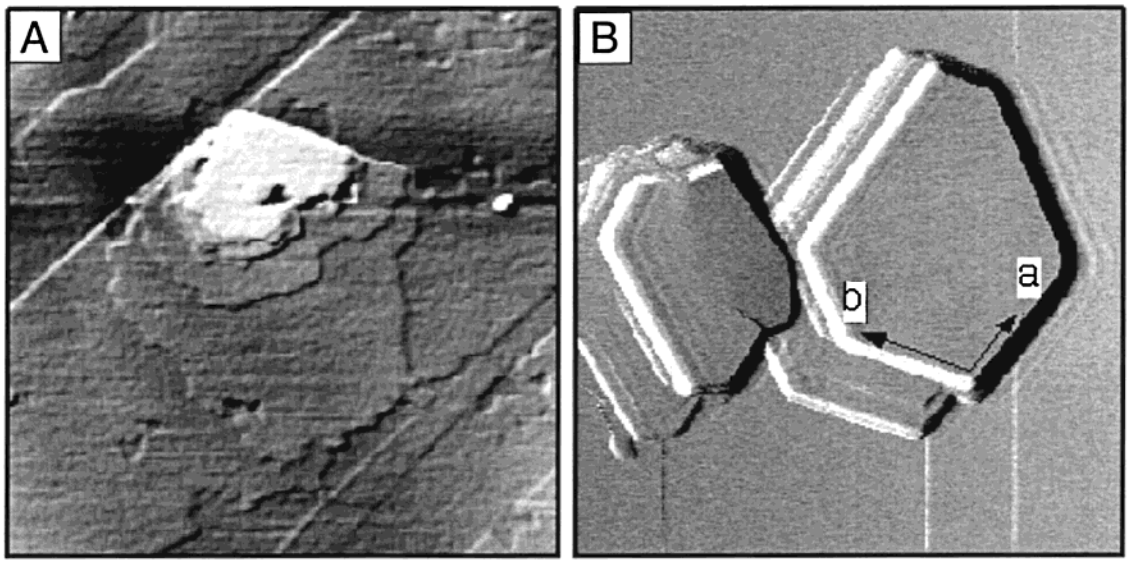

Figure 29. (a) AFM image illustrating the layer-by-layer growth of a β-$(ET)_2I_3$ (001) multilayer following formation of the first overlayer, which can be considered as a nucleation layer for the bulk crystalline phase. The layers emanate by step flow from a screw dislocation. (b) AFM image of a microscopic crystal of β-$(ET)_2I_3$ grown on HOPG directly from the β-$(ET)_2I_3$ (001) overlayer. Lattice images acquired by AFM confirmed that the large upper face was (001) with the crystallographic *a* and *b* axes oriented as shown. The *a* and *b* axes here have the same magnitude and orientation with respect to the HOPG substrate as $\mathbf{b_1}$ and $\mathbf{b_2}$ of the overlayer, respectively.

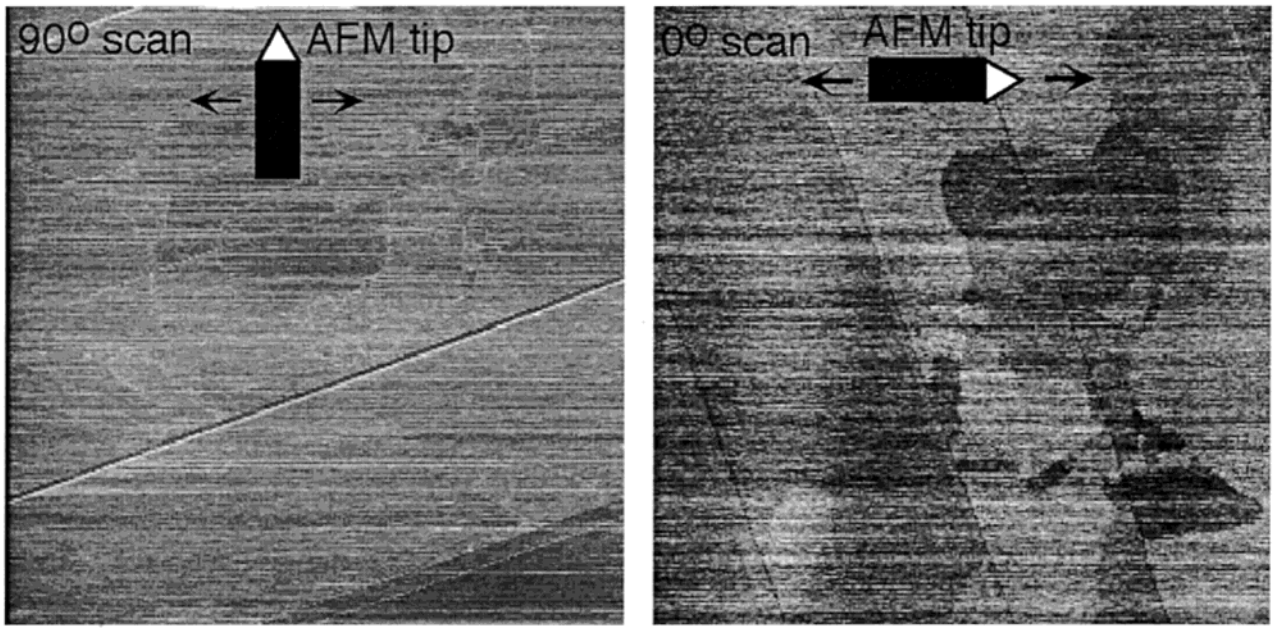

Figure 30. Lateral force images of a completely formed (001) β-$(ET)_2I_3$ overlayer with the cantilever oriented at 90° (left) and 0° (right) with respect to the scan direction (depicted by the arrows). The domain boundaries are pronounced in the 90° scan, whereas the frictional contrast of the overlayer surfaces is pronounce in the 0° scan.

This value is roughly twice that observed for the dianion, as expected based on electroneutrality. A structural model consistent with the constraints (i−iii) above can be constructed in which the unit cell contains two $MBSA^{1-}$ anions and has dimensions of $a = 8.3$ Å and $b = 19.4$ Å.

The orientation and packing density of the MBSA anions deduced from the AFM data were consistent with previously reported X-ray diffraction data obtained for HT intercalated with these anions,[102] in which the less densely packed $MBSA^{2-}$ layers can interdigitate to afford as interlayer spacing of 13 Å whereas the densely packed $MBSA^{1-}$ layers cannot interdigitate, resulting in an interlayer spacing of 21 Å. This example demonstrates that the structure of reversibly adsorbed, organized layers of molecules can be characterized in situ by AFM, providing surface stoichiometry and adlayer symmetry and even insight into ordering in a bulk solid that is not attainable by standard diffraction techniques.

4. Organic Crystal Surfaces as Nucleation Substrates

The tendency of organic crystals to form well-defined terraces and steps that correspond to precise arrangements of molecules exposed at these topographical features provides an intriguing opportunity

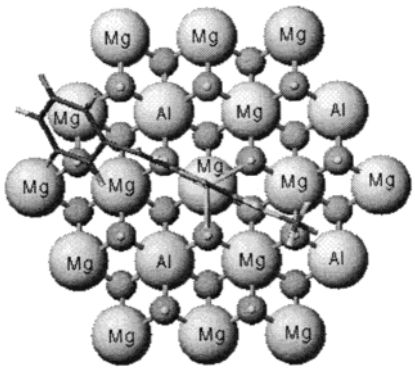

Figure 31. Schematic representation of the interaction of the MBSA anion (1− or 2−) with the HT (0001) surface via hydrogen bonding between the sulfonate moiety and a triad of hydroxyl groups that project from the HT surface. The binding to a hydroxyl triad surrounding a Mg ion depicted here is arbitrary.

to examine the organization of molecules on a diverse class of ordered substrates and to develop substrates for precise control of nucleation. Given that the number of entries in the Cambridge Stuctural Database is >150 000 and each crystal with triclinic, monoclinic, or orthorhombic symmetry has at least three independent crystal faces with different molecular structure, the number of possible substrate surfaces approaches 500 000! In fact, epitaxy at organic crystal substrate surfaces is suggested by the use of organic crystals as nucleation promotors and crystallizing aids in the manufacturing of crystalline polymers. Although the role of many of these nucleation promotors is not well understood, there has been speculation that this phenomenon is due to epitaxy between the nucleating agent and the incipient nucleus. One-dimensional epitaxy—registry between a lattice constant of the substrate and a lattice

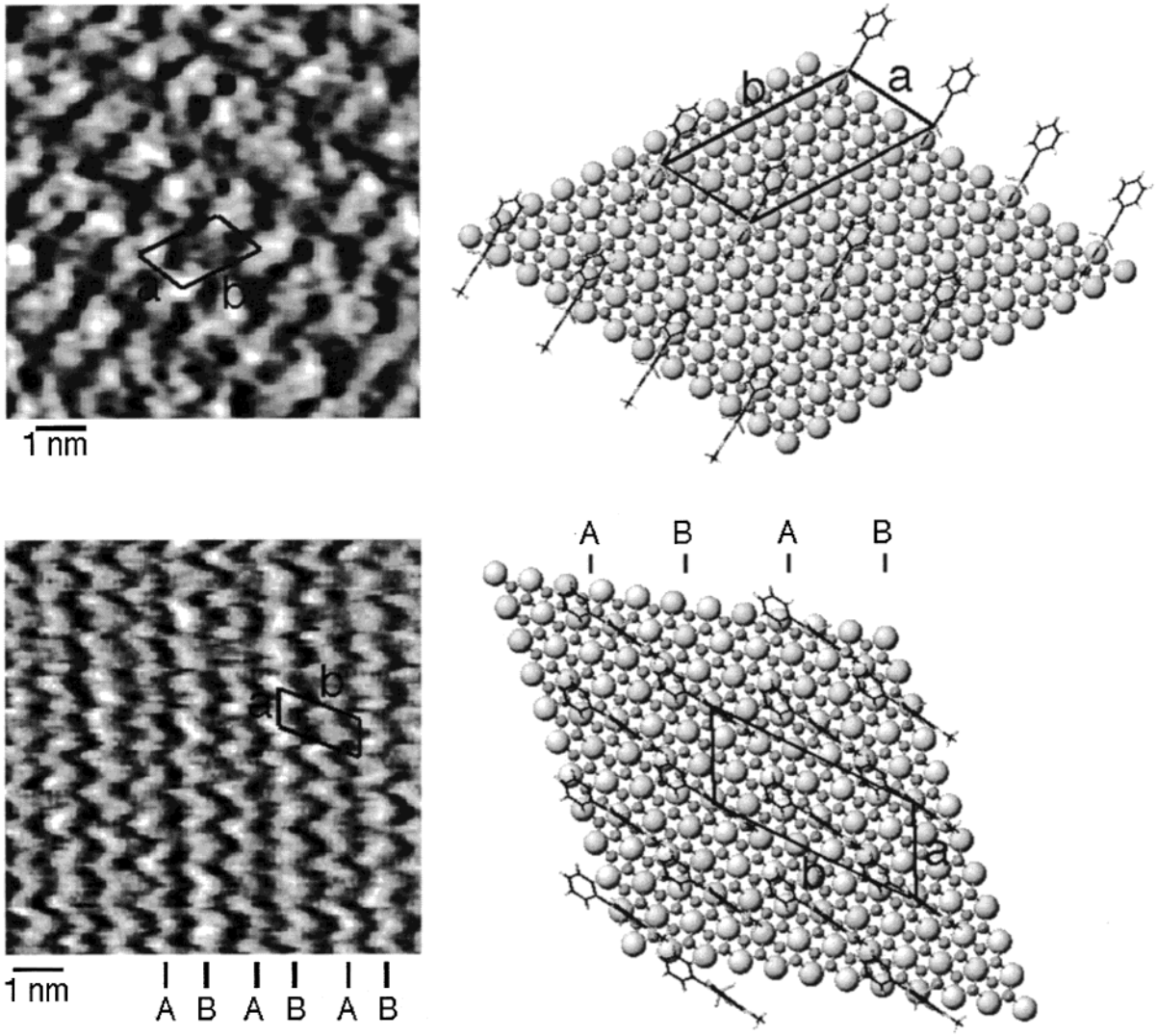

Figure 32. (upper left) AFM image of the hexagonal (0001) face of HT in an aqueous solution containing $MBSA^{2-}$ (pH = 10.5). (upper right) Model of a $MBSA^{2-}$ layer adsorbed on HT as deduced from AFM data. The lattice constants determined from the AFM data (a = 9.6 Å and b = 18.2 Å) agree with those of the model (a = 9.3 Å and b = 18.6 Å). (lower left) AFM image of the hexagonal (0001) face of HT in an aqueous solution containing $MBSA^{1-}$ (pH = 6.6). (lower right) Model of a $MBSA^{1-}$ layer adsorbed on HT as deduced from AFM data. The lattice constants determined from the AFM data (a = 8.0 Å and b = 19.3 Å) agree favorably with those of the model (a = 8.3 Å and b = 19.4 Å). In each case, the models constrain the $MBSA^{2-}$ anions to reside on hydroxyl triad sites of the HT surface while the surface coverages are consistent with electroneutrality.

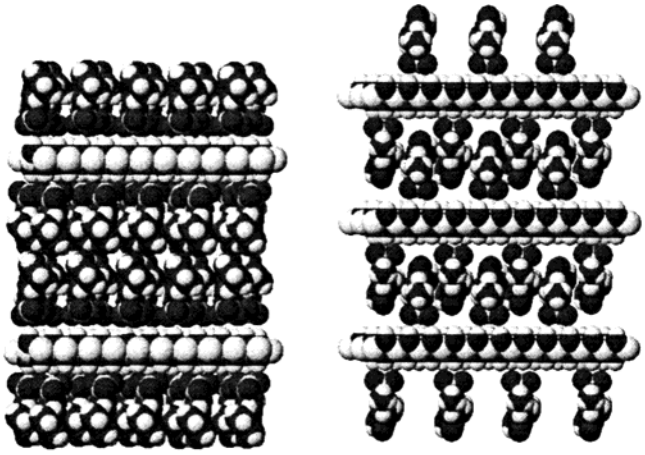

Figure 33. Molecular models of HT intercalated with $MBSA^{1-}$ (left) and $MBSA^{2-}$ (right). The less densely packed $MBSA^{2-}$ layers can interdigitate to afford an interlayer spacing of 13 Å, whereas the densely packed $MBSA^{1-}$ layers cannot interdigitate, resulting in an interlayer spacing of 21 Å. The spacings, deduced from X-ray diffractions, corroborate the coverage of the $MBSA^{n-}$ anions determined by AFM.

constant of the growing phase—has been invoked in the nucleation of crystalline polymers on a variety of organic crystal substrates.[106−113] In these cases, the polymer is considered to be commensurate along one direction only, generally through a higher order *M*:*N* commensurism where *M* and *N* are the number of polymer and substrate unit cells, respectively, and $M > N$. Epitaxy in directions perpendicular to this direction is generally not considered in these examples. This resembles the coincident epitaxy described in the previous section in that covalent bonding along the polymer chain results in a polymer elastic constant that is large compared to the elastic constant of the polymer−substrate interface along this direction. Consequently, the interfacial stresses associated with the noncoinciding positions of the polymer along the epitaxial direction do not dominate.

Interestingly, many of the molecular crystal substrates used for polymer crystallization have crystal structures with anisotropic intermolecular interactions along a well-defined direction. This will tend to favor the formation of well-defined ledges on the surfaces of these crystals that may serve as the nucleation sites for polymer crystallization. This would allow a polymer chain to contact two intersecting substrate crystal planes, a step and a terrace, that generate the ledge. While the polymer studies describe nucleation in terms of one-dimensional epitaxy, recent work in our laboratory suggests that "ledge-directed epitaxy" (LDE)[114] may be important, at least for nucleation of molecular crystals. In this case, the activation energy for nucleation is reduced by a "shape match" between crystallographically well-defined ledges of organic crystal substrates and two close-packed planes of the incipient nucleus (Figure 34).

LDE can be understood in terms of eq 13, with the free energy for nucleation, G_{tot}, reduced because of the larger A_{sn} term resulting from contact of the nucleus with two substrate planes, as compared to

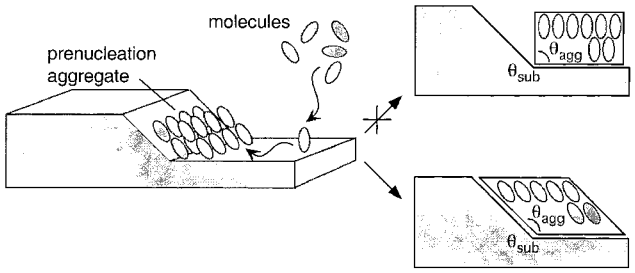

Figure 34. Schematic representation of ledge-directed epitaxy on a single-crystal substrate and the role of LDE in selective nucleation of polymorphs. The ledge is the direction defined by the line of intersection of a terrace and a step. Organization of a prenucleation aggregate and subsequent nucleation occur preferentially at the ledge site free energy lowering by contact between two planes of the incipient nucleus and the two substrate ledge planes. This requires a good geometric fit of the nucleus and the ledge site. At the upper right, ϕ_{agg} of the prenucleation aggregate does not match θ_{sub}, so nucleation of the material in this orientation or nucleation of a polymorph with this structure will not be favorable. In contrast, the lower left depicts the condition in which $\theta_{sub} = \phi_{agg}$, lowering the surface free energy of the nucleus and substrate to a greater extent so that crystallization in this orientation or nucleation of a polymorph with this structure is favorable.

contact with a single terrace plane. Well-defined ledge sites on organic substrates are preferred for materials having strong intermolecular interaction along a single crystallographic direction, such as alkane dicarboxylic acids, $HOOC-(CH_2)_n-COOH$, which organize into chains in the solid state through hydrogen bonding between carboxylic acid groups. These ledge sites exist on mature substrate crystals or can be generated in pristine form by cleaving single crystals. Cleaving generates the terrace and step planes, both containing the direction of hydrogen-bonded chains, that intersect to form the ledge. The dihedral angle (θ) between these planes is readily surmised from the crystal structure and can be verified by AFM if the angle is sufficiently large so that this determination is not limited by the tip radius. Organic crystals with strong one-dimensional intermolecular bonding, such as dicarboxylic acids, thereby provide a diverse library of substrates with different ledge angles. Three principle features distinguish LDE: (i) nucleation occurring at specific ledge sites of the crystal substrates rather than randomly on terraces, (ii) nucleation rates that are significantly enhanced in the presence of matching substrates, and (iii) crystal orientations governed by the most optimum fit between the nucleus and the ledge site ($\theta = \phi$), such that different substrates can induce different orientations. The directing influence of LDE can be very exact, with differences in ledge dihedral angles as small as one degree sufficient to alter growth orientation.

The LDE phenomena can be illustrated by the oriented growth of benzoic acid on L-valine (VAL) or succinic acid (SA), as depicted in Figure 35. Cleaved crystals of SA exhibit large $(0\bar{1}0)$ faces decorated with $[10\bar{1}]_{SA}$ ledges. These ledges are produced by the intersection of $(0\bar{1}0)_{SA}$ terraces and $(1\bar{1}1)_{SA}$ step planes, affording a substrate ledge angle of $\theta_{sub} = 112.6°$. The observed orientation of benzoic acid

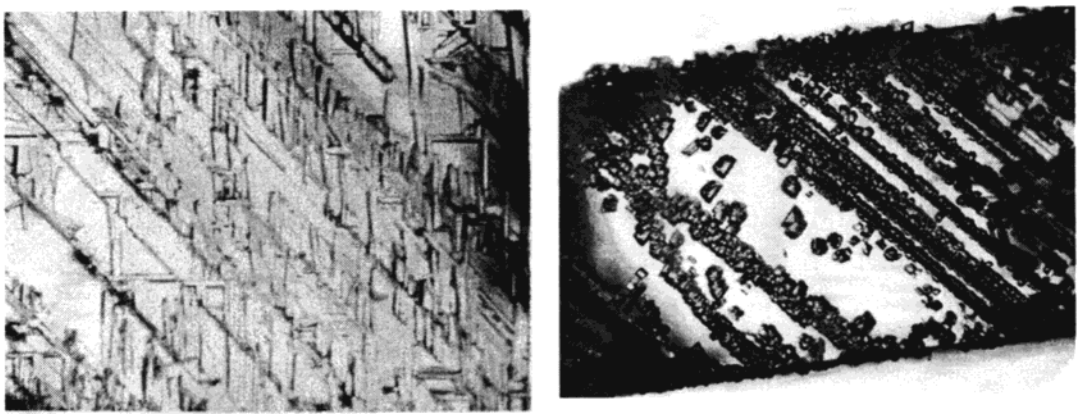

Figure 35. Photograph of benzoic acid (left) and *p*-nitroaniline (right) grown on $(0\bar{1}0)$ faces of succinic acid. Nucleation initiates at the $[10\bar{1}]_{SA}$ ledges, leading to oriented crystals decorating these ledge sites. The observed orientations are consistent with LDE-driven nucleation.

crystals indicates that nucleation is driven by contact of these two ledge planes with the benzoic acid $(001)_{BA}$ and $(112)_{BA}$ planes during nucleation, respectively. The angle between these two BA planes is $\phi_{agg} = 113.2°$. Both the ledge planes and the benzoid acid planes are densely packed so as to maximize interaction with the substrate ledge planes. Similarly, cleaved crystals of L-valine exhibited large (001) faces decorated with $[010]_{VAL}$ ledges produced by the intersection of $(001)_{VAL}$ terraces and $(201)_{VAL}$ steps, affording a ledge angle of $\theta_{sub} = 111.2°$. Even though this ledge angle was only 1.4° less than the SA ledge angle, this difference was sufficiently large to induce a different orientation in the benzoic acid crystals that grew from these ledges. In this case, the $(001)_{BA}$ and $(102)_{BA}$ planes, which intersect at an angle of $\phi_{agg} = 111.1°$, contact the $(001)_{VAL}$ terraces and $(201)_{VAL}$ steps, respectively.

LDE can be used to control polymorphism, as demonstrated for the organic dye $(DMTC^+)(TMO^-)\cdot CHCl_3$ (DMTC = 3,3′-dimethylthiacarbocyanine, TMO = 3,3′,5,5′-tetramethyltrimethine oxonol).[115] Whereas crystallizations from chloroform principally afforded three polymorphs, nucleation of a single, less thermodynamically preferred polymorph was observed at exposed $[10\bar{1}]_{SA}$ ledge sites of freshly cleaved succinic acid crystals. The crystal structures, known for two polymorphs designated as **Ia** and **Ib**, reveal that polymorph **Ib** contained aggregates defined by close-packed $(010)_{Ib}$ and $(014)_{Ib}$ planes subtending an angle of $\phi_{agg} = 113.0°$, nearly identical to $\theta_{sub} = 112.6°$ for the $[10\bar{1}]_{SA}$ ledge. In contrast, polymorph **Ia** does not possess any identifiable aggregate with a dihedral angle near this value. The orientation of **Ib** crystals, confirmed by X-ray diffraction and AFM, indicates that the close-packed $(010)_{Ib}$ and $(014)_{Ib}$ planes of a prenucleation aggregate contact the $(0\bar{1}0)_{SA}$ and $(1\bar{1}1)_{SA}$ ledge planes, respectively (Figure 36). This orientation allows both planes of the incipient nucleus of polymorph **Ib** to contact the ledge site during nucleation, thereby lowering its free energy and driving its nucleation.

These observations demonstrate that LDE can drive nucleation in the absence of conventional 2-D epitaxy, which relies on lattice matching between two lattice constants of the substrate and two lattice

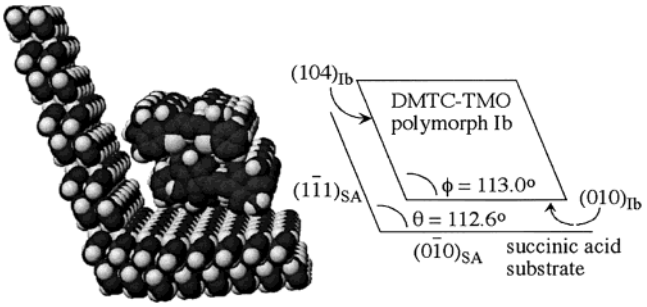

Figure 36. Molecular model of an aggregate of DMTC-TMO (polymorph **1b**) contacting the $[10\bar{1}]_{SA}$ ledge at the initial stages of nucleation. The orientation depicted here is identical to that of bulk crystals that grow from these nuclei at the ledge site. In this orientation the $(010)_{Ib}$ and $(014)_{Ib}$ planes are in contact with $(0\bar{1}0)_{SA}$ and $(111)_{SA}$, respectively, and $[100]_{Ib}$ is parallel to the $[10\bar{1}]_{SA}$ ledge. The value of $\theta_{agg} = 113.0°$ for $(01\bar{4})_{Ib} \cap (010)_{Ib}$ is nearly identical to $\theta_{sub} = 112.6°$ for the $[10\bar{1}]_{SA}$ ledge.

constants of the nucleus. Furthermore, LDE occurred even when the lattice mismatch along the ledge direction approached 5%. This approach to controlling nucleation has considerable versatility as it suggests that a library of organic seeds can be used to control polymorphism or to search for unknown polymorphs. It also illustrates that strategies for controlling nucleation must look beyond conventional approaches based on simply commensurism or stereochemical recognition.

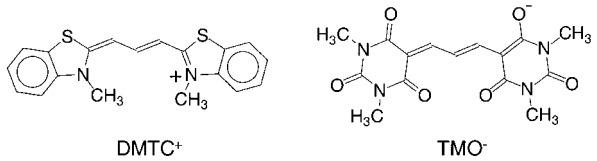

The role of organic crystal surfaces as epitaxial substrates was also suggested in studies of the nucleation and growth of *R,S*-alanine from saturated solutions in the presence of small amounts of *S*-threonine or *S*-phenylalanine.[116] The alanine crystals grown in the presence of these auxiliaries were reported to result in the formation of propeller-shaped crystals. This was attributed to twinning and fast crystal growth outward from the center of the

propeller. When performed in the presence of *R*-threonine or *R*-phenylalanine, the crystals exhibited the twinned morphology but of the enantiomorphous form. The observation of twinned *R*,*S*-alanine crystals was explained by preferential binding of the auxiliaries for the nuclei of the racemic form and only one of the enantiomers. For example, an *R*-amino acid would only bind to aggregates of the *R*,*S* and *R* forms of alanine, thereby preventing their growth. The auxiliary would bind to the *S* aggregates to a lesser extent and would not prevent their growth into viable *S* nuclei, which could then serve as templates for epitaxial growth of the *R*,*S* twins. Because these twins grow from opposite sides of the *S* nucleus with each half growing along the $-c$ direction, a chiral propeller-shaped twin is observed. This mechanism was corroborated by X-ray diffraction performed with a narrow X-ray beam so that reflections from the chiral nucleus could be observed. This work further illustrates of the role played by microscopic nuclei in nucleation and growth.

IV. Concluding Remarks

Through examples, this review has illustrated the advances in the past decade in the characterization of crystal interfaces and organized molecular arrays with scanning probe microscopy. The capabilities of AFM to probe the surface topography of crystals, including soft organic materials and interfaces, provide a general approach to determining interface structure. The ability to measure dynamics of interface formation during crystal growth, coupled with the ability to obtain lattice images, enables assignment of growth events to specific crystallographic planes so that the crucial molecular recognition events can be surmised on the near-molecular scale. The combination of interface structure characterization, kinetic measurements, and bulk single-crystal X-ray diffraction enables elucidation of these events. This molecular-level understanding will ultimately lead to the strategies for the rational manipulation of interface structure and inherent crystal properties. These insights are already leading to new strategies for controlling nucleation of crystalline phases, which has been an elusive goal for those interested in the synthesis of specific polymorphs and thin crystalline films. The author hopes that this paper encourages others to use these approaches, as well as develop related ones, so that the molecular properties of these organized interfaces can be exploited to their fullest.

V. Acknowledgments

The author is grateful for the financial support of the National Science Foundation and the Office of Naval Research and the contributions of former graduate students and postdoctoral associates, including Dr. L. M. Frostman, Dr. A. C. Hillier, Dr. D. E. Hooks, Dr. J. A. Last, Dr. W. Li, Dr. G. Z. Mao, Dr. V. A. Russell, and Dr. C. M. Yip.

VI. References

(1) Desiraju, G. R. *Crystal engineering. The design of organic solids*; Elsevier: Amsterdam, 1989.
(2) Scaringe, R. P. *Electron Crystallography of Organic Molecules*; Kluwer Press: Norwell, MA, 1991; p 85.
(3) Russell, V. A.; Ward, M. D. *Chem. Mater.* **1996**, *8*, 1654.
(4) Marsh, R. E. *Acta Crystallogr.* **1958**, 11, 654.
(5) (a) Russell, V. A.; Etter, M. C.; Ward, M. D. *J. Am. Chem. Soc.* **1994**, *116*, 1941. (b) Russell, V. A.; Ward, M. D. *Acta Crystallogr.* **1996**, *B52*, 209−214. (c) Russell, V. A.; Evans, C.; Li, W.; Ward, M. D. *Science* **1997**, *276*, 575. (d) Swift, J. A.; Pivovar, A. M.; Reynolds, A. M. *J. Am. Chem. Soc.* **1998**, *24*, 5887. (e) Evans, C. C.; Sukarto, L.; Ward, M. D. *J. Am. Chem. Soc.* **1999**, *121*, 320.
(6) Landau, E. M.; Grayer Wolf, S.; Levanon, M.; Leiserowitz, L.; Lahav, M.; Sagiv, J. *J. Am. Chem. Soc.* **1989**, *111*, 1436.
(7) Weissbuch, I.; Addadi, L.; Lahav, M.; Leiserowitz, L. *Science* **1991**, *253*, 637.
(8) Landau, E. M.; Grayer Wolf, S.; Sagiv, J.; Deutsch, M.; Kjaer, K.; Als-Nielsen, J.; Leiserowitz, L. *Pure Appl. Chem.* **1989**, *61*, 673.
(9) Gidalevitz, D.; Feidenhans'l, R.; Smilgies, D. M.; Leiserowitz, L. *Surf. Rev. Lett.* **1997**, *4*, 721.
(10) Gidalevitz, D.; Feidenhans, R.; Leiserowitz, L. *Angew. Chem., Int. Ed. Engl.* **1996**, *36*, 959.
(11) Gidalevitz, D.; Feidenhans'l, R.; Matlis, S.; Smilgies, D.-M.; Christensen, M. J.; Lieserowitz, L. *Angew. Chem., Int. Ed. Engl.* **1997**, *36*, 955.
(12) Edgar, R.; Schultz, T. M.; Rasmussen, F. B.; Feidenhans'l, R.; Leiserowitz, L. *J. Am. Chem. Soc.* **1999**, *121*, 632.
(13) Majewski, J.; Edgar, R.; Popovitz-Biro, R.; Kjaer, K.; Bouwman, W. G.; Als-Nielsen, J.; Lahav, M.; Leiserowitz, L. *Angew. Chem., Int. Ed. Engl.* **1995**, *34*, 649.
(14) Weinbach, S. P.; Weissbruch, I.; Kjaer, K.; Bouwman, W. G.; Nielsen, J. A.; Lahav, M.; Leiserowitz, L. *Adv. Mater.* **1995**, *7*, 857.
(15) Weissbuch, I.; Berfeld, M.; Bouwman, W.; Kjaer, K.; Als-Nielsen, J.; Lahav, M.; Leiserowitz, L. *J. Am. Chem. Soc.* **1997**, *119*, 933.
(16) Sirota, E. B. *Langmuir* **1997**, *13*, 3849.
(17) Weissbuch, I.; Baxter, P. N. W.; Kuzmenko, I.; Cohen, H.; Cohen, S.; Kjaer, K.; Howes, P. B.; Als-Nielsen, J.; Lehn, J.-M.; Leiserowitz, L.; Lahav, M. *Chem. Eur. J.* **2000**, *6*, 725.
(18) Li, S.; White, H. S.; Ward, M. D. *J. Phys. Chem.* **1992**, *96*, 9014.
(19) Li, S.; White, H. S.; Ward, M. D. *Chem. Mater.* **1992**, *4*, 1082.
(20) Hossick-Schott, J. H.; Ward, M. D. *J. Am. Chem. Soc.* **1994**, *116*, 6806.
(21) Dvorak, M. A.; Ward, M. D. *Chem. Mater.* **1994**, *6*, 1386.
(22) Maganov, S. N.; Kempf, S.; Rotter, H.; Cantow, H. J. *Synth. Met.* **1991**, *40*, 73.
(23) Fainchtein, R.; Murphy, J. C. *J. Vac. Sci. Technol. B* **1992**, *9*, 1013.
(24) Binnig, G.; Quate, C. F.; Gerber, C. *Phys. Rev. Lett.* **1986**, *56*, 930.
(25) Cleveland, J. P.; Manne, S.; Bocek, D.; Hansma, P. K. *Rev. Sci. Instrum.* **1993**, *64*, 403.
(26) Israelachvilli, J. *Intermolecular and Surface Forces*; Academic Press: New York, 1992.
(27) Weisenhorn, A. L.; Hansma, P. K.; Albrecht, T. R.; Quate, C. F. *Appl. Phys. Lett.* **1990**, *56*, 1758.
(28) *Scanning Tunneling Microscopy and Spectroscopy*; Bonnell, D. A., Ed.; VCH Publishers: New York, 1993.
(29) The Hamaker constants for this example were calculated using the following values: Si_3N_4 ($\epsilon = 7.5$, $n = 2.0$), HOPG ($\epsilon = 5.5$, $n = 2.4$), air ($\epsilon = 1$, $n = 1$), ethanol ($\epsilon = 24.3$, $n = 1.36$), $h\omega = 2.5 \times 10^{-18}$ J, $T = 298$ K.
(30) Hutter, J. L.; Bechhoefer, J. *J. Appl. Phys.* **1993**, *73*, 4123.
(31) Mate, C. M.; McClelland, G. M.; Erlandsson, R.; Chiang, S. *Phys. Rev. Lett.* **1987**, *59*, 1942.
(32) Yuba, T.; Kakimoto, M.; Imai, Y.; Shigeno, M. *Chem. Lett.* **1993**, *1*, 1635.
(33) Nysten, B.; Legras, R.; Costa, J. L. *Appl. Phys.* **1995**, *78*, 5953.
(34) Smithson, R. L. W.; Evans, D. F.; Monfils, J. D.; Guire, P. E. *Colloids Surf. B* **1993**, *1*, 349.
(35) Overny, R. M.; Takano, H.; Fujihira, M.; Paulus, W.; Ringsdorf, H. *Phys. Rev. Lett.* **1994**, *72*, 3546.
(36) Last, J. A.; Ward, M. D. *Adv. Mater.* **1996**, *8*, 730.
(37) Wong, S.-S.; Takano, H.; Porter, M. D. *Anal. Chem.* **1998**, *70*, 5209.
(38) (a) Carter, P. W.; Hillier, A. C.; Ward, M. D. *J. Am. Chem. Soc.* **1994**, *116*, 944−953. (b) Hillier, A.; Ward, M. D. *Science* **1994**, *268*, 1261.
(39) Mao, G. Z.; Lobo, L.; Scaringe, R.; Ward, M. D. *Chem. Mater.* **1997**, *9*, 773.
(40) Manne, S.; Cleveland, J. P.; Stucky, G. D.; Hansma, P. K. *J. Cryst. Growth* **1993**, *130*, 333.
(41) Yip, C. M.; Ward, M. D. *Biophys. J.* **1996**, *71*, 1071.
(42) Land, T. J.; Malkin, A. J.; Kuznetsov, Y. G.; McPherson, A.; De Yoreo J. J. *Phys. Rev. Lett.* **1995**, *75*, 2774.
(43) Malkin, A. J.; Kuznetsov, Y. G.; Glantz, W.; McPherson, A. *J. Phys. Chem.* **1996**, *100*, 11736.
(44) Malkin, A. J.; Land, T. J.; Kuznetsov, Y. G.; McPherson, A.; De Yoreo, J. J. *Phys. Rev. Lett.* **1995**, *75*, 2778.

(45) Balibar, F. *The Science of Crystals*; McGraw-Hill: New York, 1993; p 59.
(46) Macpherson, J. V.; Unwin, P. R.; Hillier, A. C.; Bard, A. J. *J. Am. Chem. Soc.* **1996**, *118*, 6445.
(47) (a) Land, T. A.; De Yoreo, J. J.; Martin, T. L. *Kristallografiya* **1999**, *44*, 704. (b) de Vries, S. A.; Goedtkindt, P.; Bennett, S. L.; Huisman, W. J.; Zwanenburg, M. J.; Smilgies, D.-M.; De Yoreo, J. J.; van Enckevort, W. J. P.; Bennema, P.; Vlieg, E. *Phys. Rev. Lett.* **1998**, *80*, 2229. (c) De Yoreo, J. J.; Land, T. A.; Rashkovich, L. N.; Onischenko, T. A.; Lee, J. D.; Monovskii, O. V.; Zaitseva, N. P. *J. Cryst. Growth* **1997**, *182*, 442.
(48) (a) Belcher, A. M.; Wu, X. H.; Christensen, R. J.; Hansma, P. K. *Nature* **1996**, 381, 56. (b) Teng, H. H.; Dove, P. M. *Am. Mineral.* **1999**, *782*, 878. (c) Walters, D. A.; et al. *Biophys. J.* **1997**, *72*, 1425. (d) Sikes, C. S.; Yeung, M. L.; Wheeler, A. P. *Surface Reactive Peptides and Polymers: Discovery and Commercialization*; Sikes, C. S., Wheeler, A. P., Eds.; American Chemical Society: Washington, DC, 1991; p 50.
(49) Teng, H. H.; Dove, P. M.; Orme, C. A.; De Yoreo, J. J. *Science* **1998**, *282*, 724.
(50) Land, T. A.; De Yoreo, J. J.; Lee, J. D. *Surf. Sci.* **1997**, *232*, 136.
(51) Paquette, J.; Reeder, R. J. *Geochim. Cosmochim. Acta* **1995**, *59*, 735.
(52) Burton, W. K.; Carbrera, N.; Frank, F. C. *Philos. Trans. R. Soc. London Ser. A* **1951**, *243*, 299.
(53) Addadi, L.; Berkovitch-Yellin, Z.; Weissbuch, I.; van Mil, J.; Shimon, L. J. W.; Lahav, M.; Leiserowitz, L. *Angew. Chem. Int Ed. Engl.* **1985**, *24*, 466.
(54) Lahav M.; Leiserowitz L. *NATO ASI Ser. C* **1996**, *480*, 331.
(55) Weissbuch I.; Popovitz-Biro R.; Lahav M.; Leiserowitz L. *Acta Crystallogr. Sect B: Struct. Sci.* **1995**, *B51*, 115.
(56) Markman, O.; Elias, D.; Addadi, L.; Cohen, I. R.; Berkovitch-Yellin, Z. *J. Crystal. Growth* **1992**, *122*, 344.
(57) Hanein, D.; Geiger, B.; Addadi, L. *Science* **1994**, *263*, 1413.
(58) Perl-Treves, D.; Kessler, N.; Izhaky, D.; Addadi, L. *Chem. Biol.* **1996**, *3*, 567.
(59) Perl-Treves, D.; Kam, M.; Addadi, L. *Mol. Cryst. Liq. Cryst. Sci. Technol. Sect A* **1996**, *278*, 1.
(60) Kam, M.; Perl-Traves, D.; Sfez, R.; Addadi, L. *J. Mol. Recognit.* **1994**, *7*, 257.
(61) Weissbuch, I.; Leiserowitz, L.; Lahav, M. *Adv. Mater.* **1994**, *6*, 952.
(62) Addadi, L.; Weinstein, S.; Gati, E.; Weissbuch, I.; Lahav, M. *J. Am. Chem. Soc.* **1982**, *104*, 4610.
(63) Popovitz-Biro, R.; Majewski, J.; Margulis, L.; Cohen, S.; Leiserowitz, L.; Lahav, M. *Adv. Mater.* **1994**, *6*, 956.
(64) (a) Kuznetsov, Y. G.; Malkin, A. J.; Land, T. A.; DeYoreo, J. J.; Barba, A. P.; Konnert, J.; McPherson, A. *Biophys. J.* **1997**, *72*, 2357. (b) Malkin, A. J.; Kuznetsov, Y. G.; McPherson, A. *J. Struct. Biol.* **1996**, *117*, 124. (c) Land, T. J.; Malkin, A. J.; Kutznesov, Y. G.; McPherson, A.; DeYoreo, J. J. *J. Crystal Growth.* **1996**, *166*, 893. (d) McPherson, A.; Malkin, A. J.; Kuznetsov, Y. G.; Koszelak. S. *J. Cryst. Growth.* **1996**, *168*, 74. (e) Walz, T.; Tittmann, P.; Fuchs, K. H.; Müller, D. J.; Smith, B. L.; Agre, P.; Gross, H.; Engel, A. *J. Mol. Biol.* **1996**, *264*, 907. (f) Konnert, J. H.; D'Antonio, P. and Ward, K. B. *Acta Crystallogr.* **1994**, *D50*, 603. (g) Durbin, S. D.; Feher, G. *Annu. Rev. Phys. Chem.* **1996**, *47*, 171. (h) Yip, C. M.; Brader, M. L.; DeFelippis, M. R.; Ward, M. D. *Biophys. J.* **1998**, *74*, 2199. (i) Yip, C. M.; Ward, M. D. *Biophys. J.* **1996**, *71*, 1071. (j) Yip, C. M.; DeFelippis, M. R.; Frank, B. H.; Brader, M. L.; Ward, M. D. *Biophys. J.* **1998**, *75*, 1172. (k) Durbin, S. D.; Carlson, W. E. *J. Cryst. Growth* **1992**, *122*, 71. (l) Land, T. A.; De Yoreo, J. J. *J. Cryst. Growth* **2000**, *208*, 623. (m) Land, T. A.; De Yoreo, J. J.; Lee, J. D. *Surf. Sci.* **1997**, *384*, 136. (n) Kuznetsov, Yurii G.; Konnert, John; Malkin, Alexander J.; McPherson, Alexander. Malkin, Alexander J.; Kuznetsov, Yurii G.; Lucas, Robert W.; McPherson, Alexander. *J. Struct. Biol.* **1999**, *127*, 35. (o) Kuznetsov, Yu. G.; Malkin, A. J.; McPherson, A. *J. Cryst. Growth* **1999**, *196*, 489. (p) Malkin, A. J.; Kuznetsov, Yu. G.; McPherson, A. *J. Cryst. Growth* **1999**, *196*, 471. (q) Malkin, A. J.; Kuznetsov, Yu. G.; McPherson, A. *Surf. Sci.* **1997**, *393*, 95. (r) Ng, Joseph D.; Kuznetsov, Yurii G.; Malkin, Alexander J.; Keith, Gerard; Giege, Richard; McPherson, Alexander. *Nucleic Acids Res.* **1997**, *25*, 2582.
(65) (a) Tiller, W. A. *The Science of Crystallization: Microscopic Interfacial Phenomena*; Cambridge University Press: Ithaca, NY, 1991. (b) Tiller, W. A. *The Science of Crystallization: Macroscopic Phenomena and Defect Generation*; Cambridge University Press: Ithaca, NY, 1992.
(66) Hollingsworth, M. D.; Brown, M. E.; Hillier, A. C.; Santarsiero, B. D.; Chaney, J. D. *Science* **1996**, *273*, 1355.
(67) Ward, M. D. *Curr. Opin. Colloid Interface Sci.* **1997**, *2*, 51.
(68) Toschev, S. *Crystal Growth: An Introduction*; Hartman, P., Ed.; North-Holland Publishing Company: Amsterdam, 1973.
(69) Fletcher, N. H. *J. Chem. Phys.* **1963**, *38*, 237.
(70) Tiller, W. A. *The Science of Crystallization: Microscopic Interfacial Phenomena*; Cambridge University Press: New York, 1991.
(71) Landau, E. M.; Wolf, S. G.; Levanon, M.; Leiserowitz, L.; Lahav, M.; Sagiv, J. *J. Am. Chem. Soc.* **1989**, *111*, 1436.
(72) Weissbuch, I.; Frolow, F.; Addadi, L.; Lahav, M.; Leiserowitz, L. *J. Am. Chem. Soc.* **1990**, *112*, 7718.
(73) Weissbuch, I.; Berkovic, G.; Yam, R.; Als-Nielsen, J.; Kjaer, K.; Lahav, M. *J. Phys. Chem.* **1995**, *99*, 6036−6045.
(74) Bruce, L. A.; Jaeger, H. *Philos. Mag. A* **1978**, *37*, 337.
(75) Stabel, A.; Heinz, R.; Rabe, J. P.; Wegner, G.; De Schryver, F. C.; Corens, D.; Dehaen, W.; Sueling, C. *J. Phys. Chem.* **1995**, *99*, 8690.
(76) Heinz, R.; Stabel, A.; Rabe, J. P.; Wegner, G.; De Schryver, F. C.; Corens, D.; Dehaen, W.; Suling, C. *Angew. Chem., Int. Ed. Engl.* **1994**, *33*, 2080.
(77) Muller, H.; Petersen, J.; Strohmaier, R.; Gompf, B.; Eisenmenger, W.; Vollmer, M. S.; Effenberger, F. *Adv. Mater.* **1996**, *8*, 733.
(78) Hillier, A. C.; Maxson, J. B.; Ward, M. D. *Chem. Mater.* **1994**, *6*, 2222.
(79) Cincotti, S.; Rabe, J. P. *Supramol. Sci.* **1994**, *1*, 7.
(80) Patrick, D. L.; Cee, V. J.; Beebe, T. P., Jr. *J. Phys. Chem.* **1996**, *100*, 8478.
(81) Patrick, D. L.; Cee, V. J.; Beebe, T. P., Jr. *Science* **1994**, *265*, 231.
(82) Hoshino, A.; Isoda, S.; Kurata, H.; Kobayashi, T. *J. Appl. Phys.* **1994**, *76*, 4113.
(83) Ludwig, C.; Gompf, B.; Petersen, J.; Strohmaier, R.; Eisenmenger W. *Z. Phys. B* **1994**, *93*, 365.
(84) Forrest, S. R.; Burrows, P. E.; Haskal, E. I.; So, F. F. *Phys. Rev. B* **1994**, *49*, 11309.
(85) Ludwig, C.; Gompf, B.; Petersen, J.; Strohmaier, R.; Eisenmenger, W. *Z. Phys. B* **1994**, *93*, 365.
(86) England, C. D.; Collins, G. E.; Schuerlein, T. J.; Armstrong, N. R. *Langmuir* **1994**, *10*, 2748.
(87) Chau, L. K.; Arbour, C.; Collins, G. E.; Nebesny, K. W.; Lee, P. A.; England, C.; Armstrong, N. R.; Parkinson, B. A. *J. Phys. Chem.* **1993**, *97*, 2690.
(88) Collins, G. E.; Williams, V. S.; Chau, L. K.; Nebesny, K. W.; England, C.; Lee, P. A.; Lowe, T.; Fernando, Q.; Armstrong, N. R. *Synth. Met.* **1993**, *54*, 351.
(89) Strohmaier, R.; Ludwig, C.; Petersen, J.; Gompf, B.; Eisenmenger, W. *Surf. Sci.* **1994**, *318*, L1181.
(90) Hillier, A. C.; Ward, M. D. *Phys Rev. B*, **1996**, *54*, 14037.
(91) Zhang, Y.; Forrest, S. R. *Phys. Rev. Lett.* **1993**, *71*, 2765.
(92) Forrest, S. R.; Zhang, Y. *Phys. Rev. B* **1994**, *49*, 11297.
(93) Hoshino, A.; Isoda, S.; Kurata, H.; Kobayashi, T. *J. Appl. Phys.* **1994**, *76*, 4113.
(94) Last, J. A.; Hooks, D. E.; Hillier, A. C.; Ward, M. D. *J. Phys. Chem. B* **1999**, *103*, 6723.
(95) Reiss, H. *J. Appl. Phys.* **1968**, *39*, 5045.
(96) van der Merwe, J. H. *Philos. Mag. A* **1982**, *45*, 127.
(97) Last, J. A.; Hillier, A. C.; Hooks, D. E.; Maxson, J. B.; Ward, M. D. *Chem. Mater.* **1998**, *10*, 422.
(98) Stabel, A.; Heinz, R.; De Schryver, F. C.; Rabe, J. P. *J. Phys. Chem.* **1995**, *99*, 505.
(99) Ohring, M. *The Materials Science of Thin Films*; Academic Press: New York, 1992.
(100) (a) Dutta, P. K.; Puri, M. *J. Phys. Chem.* **1989**, *93*, 376. (b) Hansen, H. C. B.; Taylor, R. M. *Clay Miner.* **1991**, *26*, 311.
(101) Reichle, W. T.; Kang, S. Y.; Everhardt, D. S. *J. Catal.* **1986**, *101*, 352.
(102) (a) Schmidt, P. C.; Benke, K. *Pharm. Acta Helv.* **1988**, *63*, 188. (b) Kokot, Z. *Pharmazie* **1988**, *43*, 249. (c) Fabregas, J. L.; Cucala, J. *Int. J. Pharm.* **1989**, *52*, 173.
(103) Rameswaran, M.; Rightor, E. G.; Dimotakis, E. D.; Pinnaravaia, T. J. *Proc. Int. Congr. Catal. 9th* **1988**, *2*, 783.
(104) *The Merck Index*, 11th ed.; Budavari, S., Ed.; Merck & Co., Inc.: Rahway, NJ, 1989; p 1419.
(105) European Patent 557,089.
(106) Wittman, J. C.; Lotz, B. *Polymer* **1989**, *30*, 27−34.
(107) Wittman, J. C.; Lotz, B. *Electron Crystallography of Organic Molecules*; Fryer, J. R., Dorset, D. L., Eds.; NATO Advanced Research Workshop; Kluwer: Dordrecht, 1991; p 241.
(108) Wittman, J. C.; Lotz, B. *Prog. Polym. Sci.* **1990**, *15*, 909.
(109) Grayer, V.; Lommerts, B. J.; Smith, P.; Lotz, B.; Wittman, J. C. *Polymer* **1995**, *36*, 1915.
(110) Schumacher M.; Lovinger A. J.; Agarwal, P.; Wittman, J. C.; Lotz, B. *Macromolecules* **1994**, *27*, 6956.
(111) Stocker, W.; Graff, S.; Lang, J.; Wittman, J. C.; Lotz, B. *Macromolecules* **1994**, *27*, 6677.
(112) Kopp, S.; Wittman, J. C.; Lotz, B. *Polymer* **1994**, *35*, 916.
(113) Kopp, S.; Wittman, J. C.; Lotz, B. *Polymer* **1994**, *35*, 908.
(114) Carter, P. W.; Ward, M. D. *J. Am. Chem. Soc.* **1993**, *115*, 11521.
(115) Bonafede, S.; Ward, M. D. *J. Am. Chem. Soc.* **1995**, *117*, 7853.
(116) Weissbuch, I.; Kuzmenko, I.; Vaida, M.; Zait, S.; Leiserowitz, L.; Lahav, M. *Chem. Mater.* **1994**, *6*, 1258.

CR000020J